International Journal of Impact Engineering 137 (2020) 103461

Contents lists available at ScienceDirect

International Journal of Impact Engineering

journal homepage: www.elsevier.com/locate/ijimpeng

Rapid mechanical evaluation of quadrangular steel plates subjected to localised blast loadings

Luiz Bortolan Neto[a,c,*], Michael Saleh[a,c], Vanessa Pickerd[b,c], George Yiannakopoulos[b,c], Zenka Mathys[b,c], Warren Reid[b,c]

[a] *Australian Nuclear Science and Technology Organisation (ANSTO), Locked Bag 2001, Kirrawee DC NSW 2232, Australia*
[b] *Defence Science and Technology (DST), 506 Lorimer St, Fishermans Bend, Melbourne VIC 3207, Australia*
[c] *DMTC Limited, Level 2, 24 Wakefield St, Hawthorn VIC 3122, Australia*

ARTICLE INFO

Keywords:
Vulnerability assessment
Multilayer perceptron
Artificial neural networks
Finite element Analysis
High strain-rate
Localised blast

ABSTRACT

The design of modern military and naval platforms against weapon threats is often assisted by a combination of experimental, analytical and computational simulations. These tools provide relevant insights about material reliability, mechanical performance and platform design vulnerability to support the determination of safety critical aspects, such as response to blast and fragmentation loading.

Analytical models are inherently simplified, limiting their ability to accurately model scenarios with complicated geometries and material properties, or highly non-linear loadings. Appropriate experimental and numerical modelling can overcome the limitations of analytical models but also require long lead times and high associated costs. These issues can be a point of concern for projects with strict development schedules, short time-to-solution, and limited resources.

Machine learning techniques have proven viable in the development of fast-running models for highly non-linear problems. The present work explores four models based on the Multilayer Perceptron (MLP), a type of Artificial Neural Network (ANN), for assessing the mechanical response of mild steel plates subjected to localised blast loading. Experiments combined with validated Finite Element Analysis (FEA) models provide a hybrid dataset for training ANNs. The resultant dataset is a combination of sparsely populated experimental data with a denser dataset of validated FEA simulations. The final results demonstrate the potential of ANNs to incorporate high strain-rate material response behaviour, such as that from blast loading, into optimised models that can yield timely predictions of structural response.

1. Introduction

The design of modern military and naval platforms for vulnerability to weapon threats is essential for crew safety and residual operational capability. An understanding of the response of complex structures to blast and fragmentation loading is required for enhanced vulnerability resistant design. Structural analysis of such high strain-rate events requires advanced numerical modelling and/or experimental analysis. These approaches are often effective for specific design assessment and predictions of structural response [1–11]. However, the high associated costs and large turn-around times (from design to testing and analysis) can affect the feasibility of these approaches for rapid assessments. It is thus sensible to identify rapid, high confidence solutions that can aid in the assessments of design, operational hazards, and forensic investigation from explosive loads.

Traditional analytical models [12–15] can deliver swift solutions but are better suited for simple geometries, and typical ‘yes/no’ failure assessments as they lack the ability to accurately describe localised failure. A compromised solution might be obtained by utilising machine learning techniques as they can be employed alongside established methods for accelerating the process of fully evaluating structures subjected to highly non-linear loadings. As an example, appropriate machine learning models could be used to quickly shortlist potential designs which would then be further investigated with in depth numerical modelling and experiments. One machine learning paradigm capable of offering solutions for detailed failure analyses are Artificial Neural Networks (ANNs). This technique is a computational approach inspired by early models of sensory processing of biological brains, as such it can be used to investigate the relationship between a set of inputs and outputs. A few studies have explored the efficiency of ANN

---

* Corresponding author at: Australian Nuclear Science and Technology Organisation (ANSTO), Locked Bag 2001, Kirrawee DC NSW 2232, Australia.
E-mail address: luizb@ansto.gov.au (L. Bortolan Neto).

https://doi.org/10.1016/j.ijimpeng.2019.103461
Received 22 February 2019; Received in revised form 31 October 2019; Accepted 24 November 2019

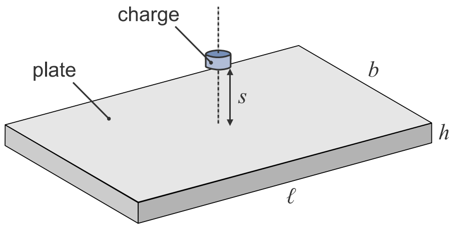

Fig. 1. Schematic of Jacob et al. [37] experiments showing mild steel plate and PE4 charge. The plate is clamped on all sides and the charge is placed at a stand-off distance *s* of 12 mm. Table 1 gives a complete list of the charge and plate dimensions considered.

based models to compute material properties [16], fatigue behaviour [17,18], fracture and impact toughness [19,20], as well as flow stress in hot deformation [21–25]. This technique was also applied to evaluate the performance of spaced aluminium armour (Whipple shields) to hypervelocity impacts from spherical projectiles [26–28]. A common limitation found in those studies is that ANNs may violate physical principles if used outside the appropriate limits as their accuracy is largely governed by the bounds of the training dataset. Ryan et al. [28] observed that ANNs can have a superior capability in reproducing complex impact phenomena when compared to Support Vector Machines (SVM). Hypothetically, other machine learning paradigms, such as Self Organising Maps and Gaussian Processes, could also be used but the literature appears to be lacking studies to verify their applicability to blast and impact events.

Training of machine learning models usually rely on field data or test trials but experimental blast testing is typically a low data environment due to cost and complexity, with many attributes poorly quantified. Resource limitations and the harsh blast testing environment make data collection relatively complicated and localised. Validated computational models have the capacity to provide supplemental data to train and improve the accuracy of machine learning implementations. This methodology has been employed to determine the propagation of blast waves in built-up environments [29–34], damage of reinforced concrete to near-field blasts [35] and the residual strength of columns subjected to blast loads [6,36], reducing the reliance solely on computational simulations. Despite demonstrating limitations that are intrinsic to ANNs, the adequate level of confidence in these applications provides a starting point for rapidly evaluating structural response to high strain-rate events.

Herein the effectiveness of the Multilayer Perceptron (MLP), a class of feedforward ANNs, for capturing the response of steel plates subjected to localised blast is investigated. Another objective is to verify the effectiveness of hybrid training datasets in which physics based numerical results enhance scarce datasets from high strain-rate test trials. Experiments from Jacob et al. [37] were combined with Finite Element Analyses (FEA) for the development of a reliable dataset and modelling framework, which allowed the authors to train the ANN models. A short description of the work of Jacob et al. [37] is given in Section 2, highlighting the test results used in this assessment. Section 3 provides further explanation of the FEA simulations employed to replicate a selection of experimental tests. The combined experimental and FEA data is then utilised to generate four different ANNs to calculate: (i) charge impulse, (ii) maximum and (iii) transient mid-plate displacements, and (iv) transient plastic strain at the plate centre. The subsequent material and structural response, validation and limitations

Table 1

Charge sizes and geometric parameters of the experimental dataset for plates exhibiting large inelastic response with thinning in the centre [37]. Asterisks (*) indicate specimens utilised for training the ANNs. The remaining samples were used for validation purposes.

No.	**Code**	**Charge (PE4)**				**Plate (mild-steel)**				
		Mass (g)	Diameter (mm)	Height (mm)	Impulse (Ns)	Yield stress (MPa)	Thickness (mm)	Breadth (mm)	Length (mm)	Max central disp. (mm)
1	N26100150	4.2	32.0	3.0	9.7	288	1.6	160.0	160.0	27.3
2	S22090111*	9.0	64.0	2.0	17.3	288	1.6	188.2	188.2	36.3
3	N29090118*	4.5	32.0	3.2	10.2	268	2.0	160.0	160.0	22.6
4	S29090119	6.3	38.0	3.5	13.4	268	2.0	190.0	190.0	32.9
5	D21090104*	7.5	36.0	4.7	14.4	230	3.0	180.0	180.0	24.5
6	D22090104*	8.5	35.0	5.8	16.6	230	3.0	175.0	210.0	28.0
7	D28090101*	8.0	30.0	7.3	16.0	230	3.0	150.0	210.0	27.7
8	D28090104*	9.0	29.6	8.6	16.1	230	3.0	148.0	236.8	28.4
9	D04100106*	8.5	29.6	8.1	16.4	230	3.0	148.0	236.8	27.6
10	N22100143*	4.7	32.0	3.4	10.0	268	2.0	128.0	294.4	25.3
11	N22090108	4.0	32.0	2.8	9.0	288	1.6	160.0	160.0	25.7
12	N29090116*	5.0	32.0	3.7	10.4	268	2.0	160.0	160.0	24.9
13	N21090103*	8.0	32.0	6.5	16.3	230	3.0	160.0	160.0	27.9
14	N01100121*	4.0	32.0	2.8	8.8	288	1.6	128.0	294.4	23.7
15	N22100145*	3.9	32.0	2.7	8.5	288	1.6	128.0	294.4	23.4
16	N02100129	4.8	32.0	3.5	10.1	268	2.0	128.0	294.4	25.8
17	S26100148*	8.8	61.0	2.0	17.1	288	1.6	190.6	190.6	37.1
18	S26100151*	11.8	64.0	2.5	22.6	268	2.0	188.2	188.2	41.7
19	S04100131*	4.8	42.0	2.0	10.2	288	1.6	120.0	288.0	23.9
20	S04100135	5.7	42.0	2.5	12.8	268	2.0	120.0	288.0	27.1
21	S22100140	9.4	42.0	4.5	18.4	230	3.0	120.0	288.0	27.7
22	N25100136	7.5	32.0	6.0	15.0	230	3.0	128.0	294.4	26.3
23	S27100156	20.5	64.0	4.5	38.2	230	3.0	188.2	188.2	48.2
24	D22090103	7.5	35.0	5.0	14.5	230	3.0	175.0	210.0	25.0
25	D01100103	9.0	35.0	6.2	18.1	230	3.0	175.0	210.0	30.2
26	D28090102	8.5	30.0	7.9	16.6	230	3.0	150.0	210.0	28.1
27	D01100102	9.0	30.0	8.4	18.0	230	3.0	150.0	210.0	28.8
28	D26100105	10.0	30.0	9.4	17.5	230	3.0	150.0	210.0	29.5
29	D26100107	10.5	30.0	10.0	18.1	230	3.0	150.0	210.0	31.1
30	D29090104	8.0	26.6	9.8	15.0	230	3.0	133.0	239.4	23.2
31	D04100103	9.0	29.0	9.0	17.8	230	3.0	145.0	290.0	28.7
32	D26100102	9.5	29.0	9.5	19.3	230	3.0	145.0	290.0	29.3
33	D25100102	7.5	26.4	9.1	14.4	230	3.0	132.0	290.4	24.9
34	D25100103	8.0	26.4	9.8	15.4	230	3.0	132.0	290.4	26.1
35	D25100104	9.0	26.4	11.2	16.7	230	3.0	132.0	290.4	27.3

Table 2
Johnson–Cook parameters for mild steel [47].

A	B	n	C
217 MPa	234 MPa	0.6248	0.0756

Table 3
JWL EOS parameters for PE4 [53].

ρ_{e0}(kg/m3)	v_d (m/s)	P_{CJ} (GPa)	K_1 (GPa)	K_2 (GPa)	R_1	R_2	ω	E_e (MJ/kg)
1601	8193	28	609.8	12.95	4.5	1.4	0.25	5.621

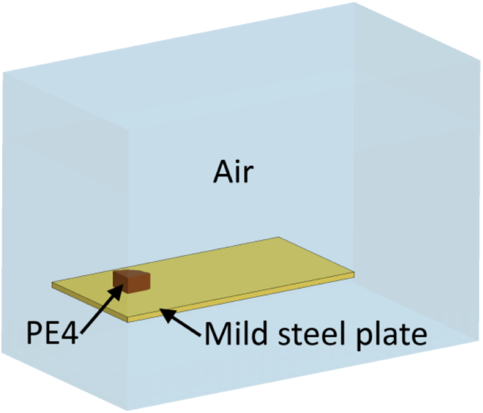

Fig. 2. Finite element blast model of the experimental set-up, including the air domain (blue), mild steel plate (yellow) and the PE4 explosive (brown). Quarter symmetry was used to reduce computational expense.

of these models are presented in Section 4. The underlying MLP theory and training techniques utilised are discussed in Appendix A.

2. Plates under localised blast

Steel plates are often utilised in the design of protective structures against dynamic loading events, such as ballistic impact and blast loading in industrial, military and civilian structural design. A number of studies analysed the deformation mechanics and failure modes of steel plates to high strain-rate loadings [38–40]. In the work of Jacob et al. [37] a series of blast tests were conducted on fully clamped mild steel plates, with a thickness-dependent static yield stress σ_y, thickness h, length ℓ and width b. The stand-off distances of the charge from the plates were consistent at $s = 12$ mm. Cylindrical plastic explosive (PE4) charges of diameter $\varnothing_c$, height h_c and mass m_c were used. Fig. 1 presents an illustration of the experimental set-up. A total of 148 specimens were tested with the plates displaying large inelastic deformation (Mode I), large inelastic response with thinning in the centre (Mode Itc), partial tearing in the centre (Mode II*c) or complete tearing in the central area (capping, Mode IIc). Pertinent metrics given by the experiments include the impulse I_c yielded by the charge and the plate mid-point displacement u_{max}. To reduce the scope for development of specific ANN models, the present work focuses only on plates exhibiting large inelastic responses with thinning in the centre (Mode Itc) as these allow for benchmarking comparisons between the final deformed structure with numerical predictions, which in turn can provide additional strain and strain-rate information. The tests that displayed such responses were used to train and validate the ANNs and are presented in Table 1.

Strain-rate and temporal displacement measurements are important for understanding structural deformation under applied blast loading. Typically, strain gauges and digital image correlation (DIC) techniques can be employed to gather temporal measurements from experiments [41–44]. However, these are not always readily available and previous studies utilising the ANNs framework [45] were unable to capture, with sufficient accuracy, the response of plates subjected to localised blast. This was attributed to the experimental dataset available lacking sufficient detail with respect to the steel's mechanical behaviour. The hypothesis presented herein contends that well established FEA methods can be used to supplement data collection when experimental data of high strain-rate events is scarce or limited.

The ANNs are applied herein through a 'replicative training' method whereby FEA results reinforce existing experimental data, increase the population pool and introduce a material strength invariant component (through constant Johnson–Cook (JC) parameters) providing additional training data. This allows for greater examination of strength effects through a number of idealised experimental analogues. The FEA models utilised for obtaining the synthetic data employed in the ANN replicative training are discussed in the next section.

3. Synthetic data from finite element models

3.1. FE Model setup

Additional data for ANN training is provided from a selection of Jacob et al. [37] experiments replicated in LS-DYNA simulations. These experiments investigated the response of clamped mild steel plates (density $\rho = 7700$ kg/m^3) to blast loading generated by PE4 charges at a 12 mm stand-off distance. Owing to the complexity (strong non-linearity) of high strain-rate events, numerical simulations can run for days in powerful computer clusters. It is thus of significant interest to run the minimum number of numerical simulations that can yield optimum improvements to the training of ANNs. A selection of ten experiments were initially modelled but proved to be insufficient to develop meaningful ANNs. A second iteration increased the selection to 20 experiments, which proved satisfactory as it became statistically representative of the larger experimental dataset. Rows 1 to 20 in Table 1 provide the relevant geometric and material information for all 20 specimens modelled.

Simulations of the experiments were used to compute the spatial and temporal variations in the plate deformation; interrogate the complex strain-rate behaviour of the steel under blast loading; and determine the resultant stress-strain contours. The high strain-rate (HSR) flow stress (σ_{eq}) was computed using a reduced version of the Johnson–Cook (JC) [46] constitutive model, given by:

$$\sigma_{eq} = (A + B\varepsilon^n)(1 + C\ln\dot{\varepsilon}^*), \tag{1}$$

where ε is the effective plastic strain, $\dot{\varepsilon}^*$ is the dimensionless plastic strain-rate and $A, B, n,$ and C are the JC material constants. This phenomenological model accounts for the yield stress increase due to strain hardening, and the rise in yield and tensile strength with increased strain-rate. The adiabatic heating term is not utilised in the current study. The material constants for mild steel (Table 2) are reproduced from the work of Vedantam et al. [47] as the data exhibits a yield strength commensurate with the stated yield strength used in the blast experiments.

Simulations of the experiments focused on the steel plate response (displacement/bulging) in "Mode Itc". Quarter symmetry was used to simplify the simulations, as illustrated by Fig. 2. The mild steel plates were fully edge-constrained and modelled using solid elements with reduced integration and hour-glassing controls to limit element locking and allow for severe elemental deformation with reduced computational cost. Arbitrary Lagrangian–Eulerian (ALE) elements were used to compute the Fluid Structure Interaction (FSI) at the explosive/air interface and the mild steel plate. The ALE domain was meshed using 8

Table 4
Experimental and FEA results for the mid-plate displacement.

No.	**Code**	Experiment		FEA		Results difference (%)
		Mid-plate displacement (mm)	Mid-plate displ.–plate thickness ratio	Mid-plate displacement (mm)	Mid-plate displ.–plate thickness ratio	
1	N26100150	27.3	17.06	27.61	17.26	+ 1.14
2	S22090111	36.3	22.69	39.06	24.41	+ 7.60
3	N29090118	22.6	11.30	23.51	11.76	+ 4.03
4	S29090119	32.9	16.45	29.79	14.90	– 9.45
5	D21090104	24.5	8.17	23.25	7.75	– 5.10
6	D22090104	28.0	9.33	26.14	8.71	– 6.64
7	D28090101	27.7	9.23	25.20	8.40	– 9.03
8	D28090104	28.4	9.47	27.19	9.06	– 4.26
9	D04100106	27.6	9.20	26.16	8.72	– 5.22
10	N22100143	25.3	12.65	24.52	12.26	– 3.08
11	N22090108	25.7	16.06	26.44	16.53	+ 2.88
12	N29090116	24.9	12.45	25.90	12.95	+ 4.02
13	N21090103	27.9	9.30	25.13	8.38	– 9.93
14	N01100121	23.7	14.81	26.56	16.60	+ 12.07
15	N22100145	23.4	14.63	25.97	16.23	+ 10.98
16	N02100129	25.8	12.90	25.04	12.52	– 2.95
17	S26100148	37.1	23.19	38.08	23.80	+ 2.64
18	S26100151	41.7	20.85	39.13	19.57	– 6.16
19	S04100131	23.9	14.94	27.10	16.94	+ 13.39
20	S04100135	27.1	13.55	25.70	12.85	– 5.17

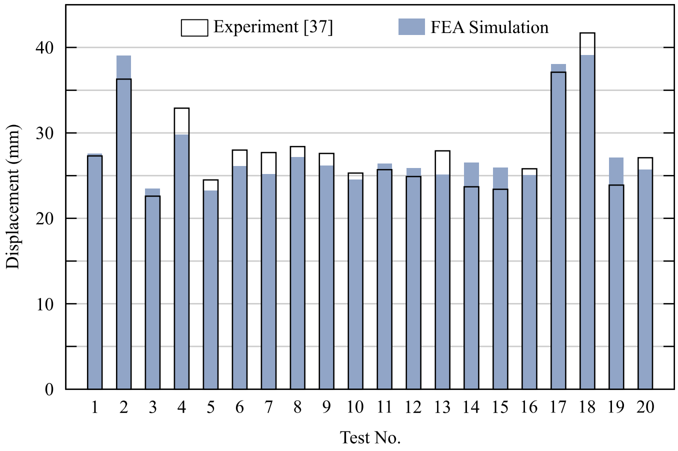

Fig. 3. Modelling results for simulation used to train ANN. A good agreement between the FE results and Jacob et al. [37] experiments was observed.

nodes and 1 point integration ALE multi-material elements.

Due to the finite computational domain, a non-reflecting boundary condition was applied to the external air boundaries and a symmetry plane was applied to the two internal ALE and solid plate boundaries. The non-reflecting boundary ensures the pressure waves are not artificially reflected back into the computational domain.

3.1.1. *Explosive*

The solid explosive is modelled using a *MAT_HIGH_EXPLOSIVE_BURN material model previously employed for the analysis of explosives in soil [48–51]. The explosive product is modelled using the Jones, Wilkins and Lee (JWL) equation of state (EOS) with the pressure term P_e given by:

$$P_e = K_1\left(1 - \frac{\omega}{R_1 V}\right)\exp(-R_1 V) + K_2\left(1 - \frac{\omega}{R_2 V}\right)\exp(-R_2 V) + \frac{\omega \rho_{e0} E_e}{V_e}, \tag{2}$$

where K_1, K_2, R_1, R_2, ω are material constants usually derived from cylindrical explosive testing or thermo-chemical kinetic simulations. V_e is the relative volume, ρ_{e0} is the initial density of the explosive and E_e is the internal specific energy per unit mass of explosive. The first term of the JWL is the high-pressure term where the relative volume is close to 1. The second intermediate pressure term applies when V_e is close to 2. As V_e becomes larger in the expanded state the EOS reduces to the last term, $\omega \rho_{e0} E_e / V_e$ [52]. The JWL parameters are analogous to those used in [53] for PE4, with a TNT equivalence of ~1.2, and are listed in Table 3. This table also gives the velocity of detonation v_d and the Chapman–Jouguet pressure P_{CJ} for PE4.

3.1.2. *Air*

The air domain was modelled using an ideal gas relation *EOS_LINEAR_POLYNOMIAL. To initialise the atmospheric pressure of 101 kPa, the relation below was used:

$$P_a = (\gamma - 1)\frac{\rho_{a0}}{\rho_a} E_a, \tag{3}$$

where P_a is the atmospheric pressure; γ is the specific heat ratio (1.4); ρ_a is the current air density; ρ_{a0} is the initial air density (1.25 kg/m^3); and E_a is the energy per unit volume (253.2 kPa).

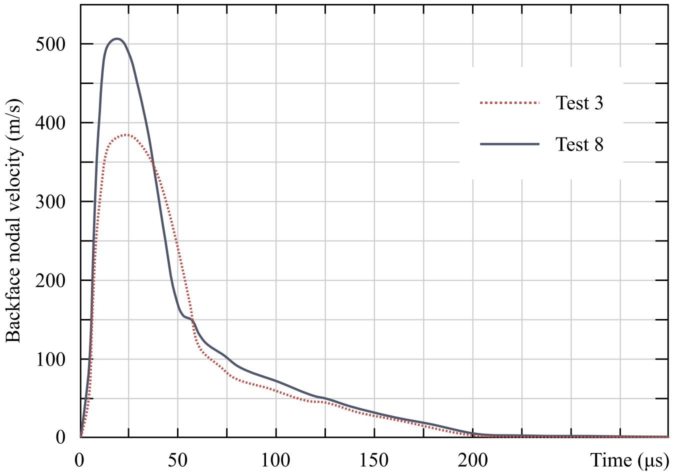

Fig. 4. Temporal variations of backface velocity for simulations Test 3 (dashed line) and Test 8 (continuous line). Charges of similar diameters were used and the different responses are due to disparities in charge height and mass; and in plate dimensions and yield strength. In both cases maximum velocity is reached at approximately 20 μs with the plate resting at about 220 μs.

3.2. FE Results

All the experiments selected for the ANNs are characterised as having large inelastic responses with thinning in the central area (Mode Itc) which was replicated in the FEA simulations. The results obtained for the mid-plate displacement are summarised in Table 4 and Fig. 3, showing good agreement of the simulations with the reported experiments; with an average reported error of 6.3% and a standard deviation of 3.4% across all 20 simulations.

The largest displacement variation between the experiments and FE results were observed for tests 14, 15 and 19. These tests had the thinnest plates in the experimental series, with a 1.6 mm thickness. However, good correlation was achieved for tests 1, 2, 11 and 17, which also used 1.6 mm thickness plates, with an average error of 3.6%. The authors hypothesise that in addition to the higher yield strength observed in thinner sheets, an effect that can be attributable to grain refinement due to rolling and the Hall–Petch relationship, through-thickness texture differences in rolled plates [54] may also affect the results through deviation of the JC parameters. Additionally, the simplified JC models and the parameters used herein may give rise to variations in the flow stress between the models and the experiment owing to the variation in the mild steel performance. Experimental errors may also play a role, and because of the idealised nature of the simulations, small nuanced differences in the experiments are not reflected in the FE models.

The maximum velocities of the mild steel plate for Test 3 and Test 8 are attained at approximate time $t = 20$ μs and are in excess of 500 m/s for Test 8 and 380 m/s for Test 3, with the velocity vectors being largely confined to the central region below the charge, as shown in Figs. 4 and 5. The charges from these tests have similar diameters and variations in the blast propagation and loading are a direct consequence of differences in

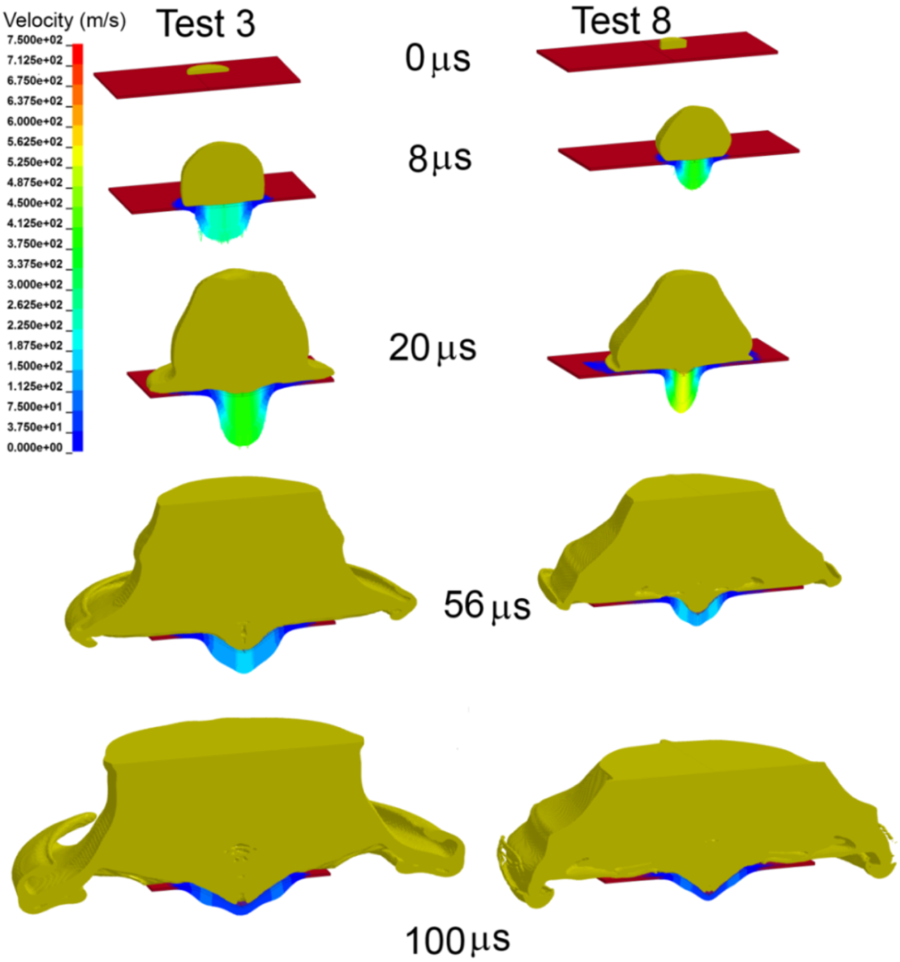

Fig. 5. Iso surface plot of blast products and back face velocity (m/s) of target plates from Test 3 and Test 8. The charges used have similar diameters with different responses attributed to variations in charge height and mass.

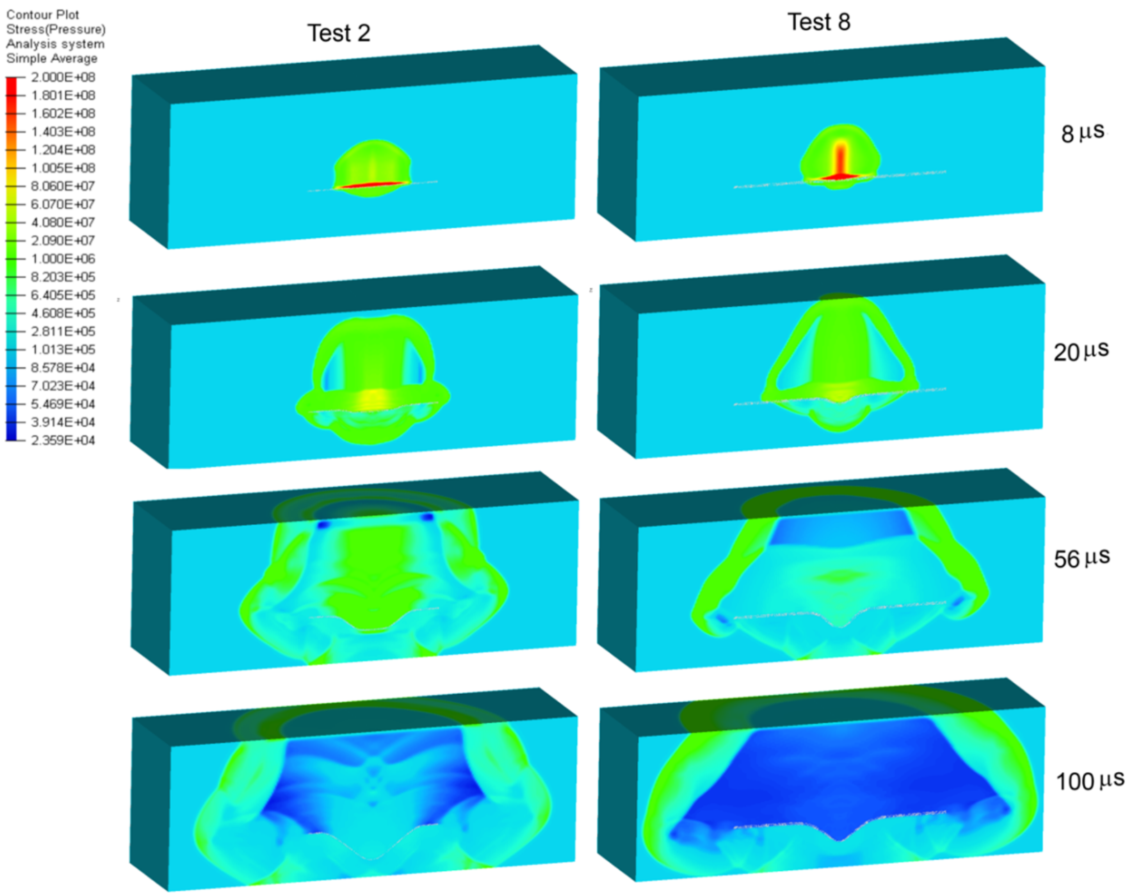

Fig. 6. Pressure plot of blast products interaction with the plates for Test 2 and Test 8. Even though the charges used have identical mass and generate similar impulse, the propagation of the blast products is highly influenced by the cylindrical charge aspect ratio. Note the vertical zone of high pressure positioned above the plate centreline at 8 μs in Test 8. This zone is not apparent in Test 2 in which the charge shape is highly flattened.

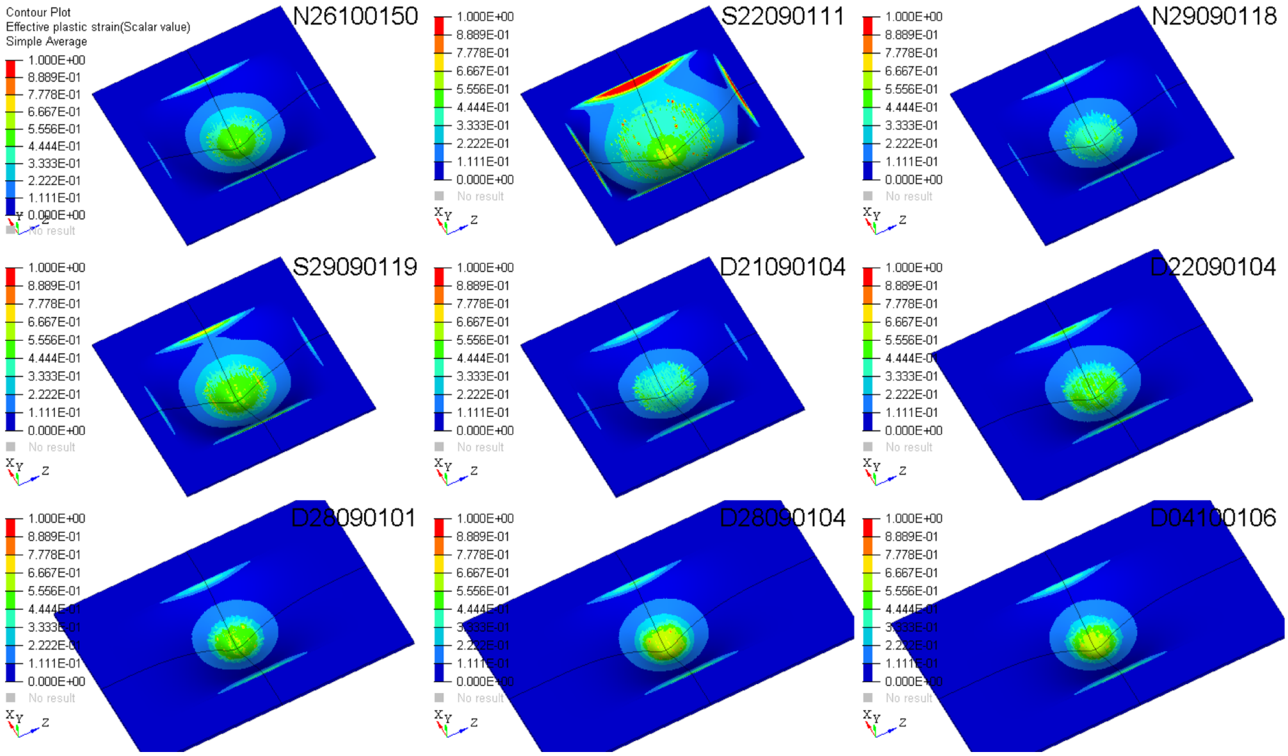

Fig. 7. Plastic strain results at $t = 200$ μs for the Tests 1 to 9 exhibiting plastic hinging for small aspect ratio plates.

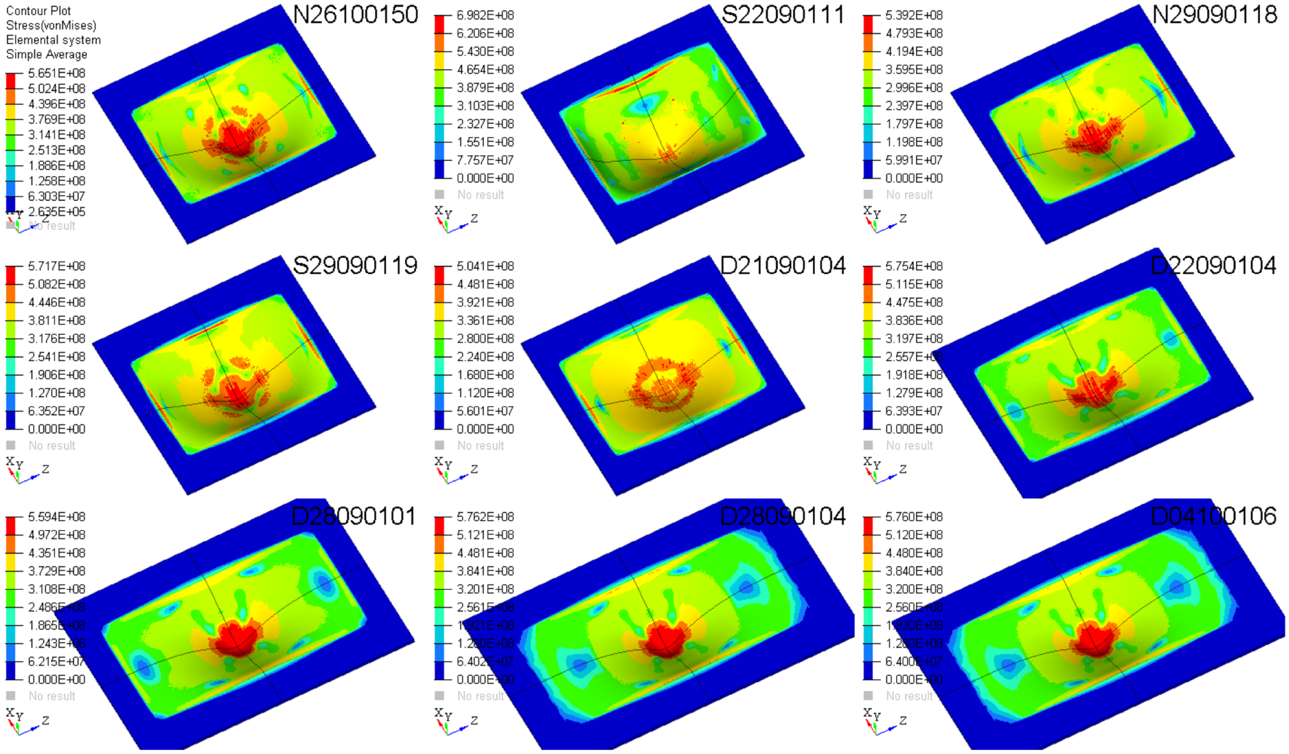

Fig. 8. Spatial distribution of von Mises stresses at $t = 200$ μs for Tests 1 to 9. Stresses are confined to the unclamped region of the plates.

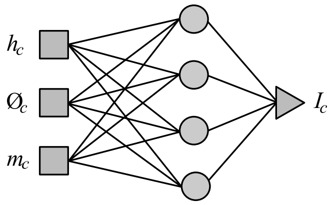

Fig. 9. Schematic of the MLP for calculating the impulse I_c due to cylindrical PE4 charges as a function of height h_c, diameter $\varnothing_c$ and mass m_c. Only one hidden layer with four artificial neurons was required to obtain reasonable predictions.

charge height and mass. Temporal variations of the FSI are seen in the isosurface of the blast products in Fig. 5, with half symmetry for Test 3 and Test 8.

Studies by Knock and Davies [55] and Hammond [56] have observed that blast waves radiating from cylindrical charges form complex patterns such as bridging waves, where the two shockwaves from the ends and sides of the cylindrical charge meet. These bridging waves are accompanied by higher shear stresses which influence the FSI. The position and the magnitude of these waves are also affected by small misalignments in the charge positions, which when combined with the directionality of the blast products may additionally contribute to any displacement variations observed.

The plastic deformation of the plate is driven by the pressure imparted on the top face by the PE4 charge and the strong FSI coupling which drives the deformation, owing to the very small stand-off distances, with a corresponding scaled distance of $Z = \varnothing_c/(2m_c^{1/3}) = 0.071$ m/kg$^{1/3}$ for Test 8. The pressure contours in Fig. 6 show a pronounced focusing effect of the pressure at $t = 8$ μs for Test 2 and Test 8. Test 8 also presents a vertical zone of high pressures positioned above the plate centreline, which is not apparent when the charge shape is highly flattened with the same charge mass – as in the case of Test 2. This is characteristic of the asymmetric propagation of cylindrical charges and is experimentally corroborated by the localised bulging and cap rupture of the experimental plates. The pressure drops significantly between $t = 56$ μs and $t = 100$ μs with the former time corresponding to the maximum back face displacement of the plate.

The regions exhibiting the largest plastic strains are those directly below the charge and at the edge of the clamped region closest to the charge, as illustrated in Fig. 7 at $t = 200$ μs. This area forms a plastic hinge which is apparent along one of the clamped edges for the large aspect plates and along two edges for the smaller aspect ratio plates. The von Mises stress contours at $t = 200$ μs, shown in Fig. 8, exhibit a range of 200–500 MPa under load with the stresses being confined to the unclamped region.

4. ANNs to predict the response of plates under localised blast

ANNs have the potential to significantly reduce the time and costs associated with the design of structures subjected to high strain-rate events by providing optimised models that might decrease the number of numerical models and experimental testing needed [57]. Four different ANN architectures were developed to estimate charge impulse (I_c), maximum mid-plate displacement ($u_{\max}$), transient mid-plate displacement ($u(t)$) and transient mid-plate strain ($\varepsilon(t)$). A 'replicative' training method, which combined the experimental data and FEA results discussed earlier in Sections 2 and 3, was utilised. This method expanded the training population and allowed for the development of ANNs dedicated to temporal parameters.

The utilisation of simplified models often leads to less accurate solutions. This becomes more apparent in highly non-linear applications, such as high strain-rate simulations. Therefore, ANN results with a maximum absolute difference of 10% from the experiments were established as benchmark, yielding predictions in the vicinity of the expected results thus providing higher confidence in the decision-making process. All four ANNs were trained with the Levenberg–Marquardt algorithm [58,59] aimed at finding the minimum configuration that would yield reasonable predictions. This minimum configuration is characterised by a Multilayer Perceptron (MLP) with a set of relevant inputs, one output and a single hidden layer for which the number of

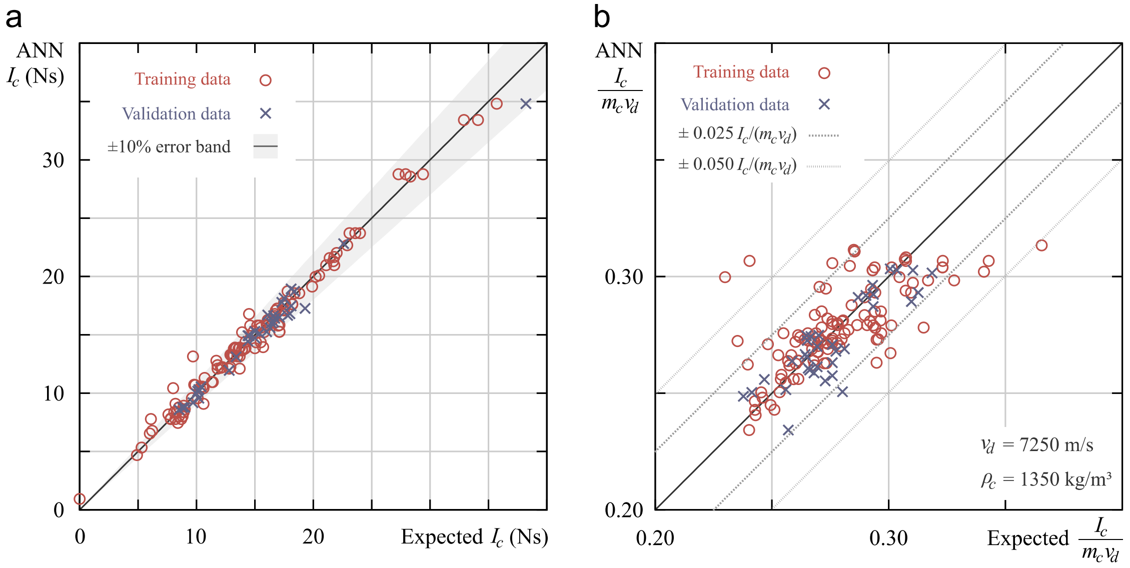

Fig. 10. Comparison between the PE4 charge impulse I_c calculated using the ANN (ordinate) and the expected values from the experiments (abscissa). The circles represent the specimens utilised to train the ANN whereas the crosses indicate the data used for validation. A good agreement is observed, with (a) most of the results being within the ± 10% error band (shaded area) and (b) the majority of the ANN results for the dimensionless PE4 charge impulse sitting inside the ± 0.050 $I_c/(m_c v_d)$ interval.

Table 5
Statistical parameters of the input data used to train and to validate the charge impulse ANN.

Input	Training dataset		Validation dataset	
	Average	Standard deviation	Average	Standard deviation
$\varnothing_c$	36.51	10.14	35.74	10.81
h_c	4.90	2.49	5.74	2.91
m_c	6.59	3.50	6.89	3.07

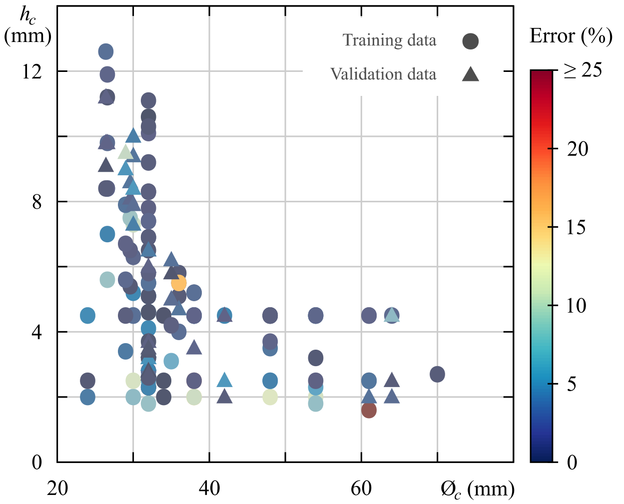

Fig. 11. Distribution of the validation data (triangles) in comparison to the training data (circles) for the charge impulse ANN. The symbols are coloured by their error in comparison to Jacob et al. [37] experiments.

neurons are minimised by trial and error. This is the simplest form of ANN [60] and its lean structure is preferable for interrogating input–output relationship when compared to other more complex types of ANN, such as Recurrent Neural Networks and Convolutional Neural Networks. Eq. (4) presents a mathematical representation of a single hidden layered MLP used herein for calculating the approximate output $\hat{y}$, where $\mathbf{\Lambda}$ is a linear transformation applied to the augmented input vector $\{1 \quad \mathbf{x}\}^T$ and the matrices $\mathbf{W}_0$ and $\mathbf{W}_1$ store the connecting weights computed in the training phase. The activation functions $\alpha_1(\cdot)$ and $g(\cdot)$ introduce nonlinearity in the models. These functions are described in Appendix A.3 by Eqs. (17) and (18), respectively.

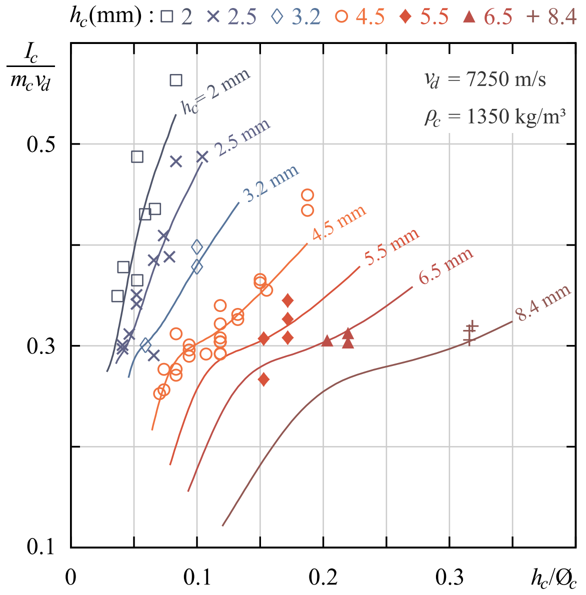

Fig. 12. The dimensionless PE4 charge impulse (ordinate) versus the charge height–diameter ratio (abscissa) for varying charge height h_c. The lines represent the ANN and the scattered symbols indicate experimental data. The ANN was very effective in finding patterns amid the experiments.

$$\hat{y} = g\left(\mathbf{W}_1\alpha_1\left(\mathbf{W}_0\Lambda\begin{Bmatrix}1\\ \mathbf{x}\end{Bmatrix}\right)\right) \tag{4}$$

The Levenberg–Marquardt algorithm was chosen because of its robustness and reliability and it was computationally implemented via the C programming language. The application of ANNs to model the response to impact and blast events is relatively recent thus a summary of the MLP theory is given in Appendix A.1. The Levenberg–Marquardt algorithm is described in Appendix A.2 and the complete formulation of

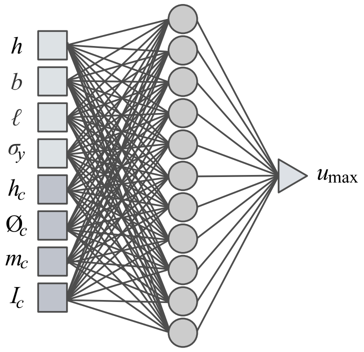

Fig. 13. Representation of the ANN for obtaining the maximum mid-plate displacement $u_{\max}$. The plate dimensions (h, b, ℓ) and yield stress σ_y were combined to the charge dimensions (h_c, $\varnothing_c$), mass m_c and impulse I_c to produce reliable estimates. Eleven artificial neurons were utilised in the single hidden layer due to the problem high non-linearity.

the ANNs discussed below are presented in Appendix A.3. A more comprehensive treatment of ANNs can be found in Refs [61–64].

4.1. Charge impulse

The charge impulse is the main driver for the plate deformation and it is shown to be one of the key parameters which the ANN models rely on to deliver fair predictions. It is thus pertinent to have an ANN dedicated to estimating the impulsive load yielded by the charge.

In their experiments, Jacob et al. [37] performed 148 tests and employed a ballistic pendulum to measure the impulsive load (I_c) generated by cylindrical PE4 charges of mass m_c. PE4 has a detonation velocity (v_d) in the range of 7000 to 7500 m/s, and density (ρ_c) of 1350 kg/m^3 [37]. Tested heights (h_c) ranged from 1.8 mm to 12.6 mm and tested diameters ($\varnothing_c$) varied from 24 mm to 70 mm. Out of the complete testing population, a subset with 113 specimens (76.35%) was used to train the ANN and the remaining 35 specimens listed in Table 1 (23.65%) were used for validation purposes.

During the training stage the number of neurons in the hidden layer was varied and it was found that an architecture consisting of three inputs ($\varnothing_c$, m_c and h_c) and one hidden layer with four neurons, as illustrated by Fig. 9, was sufficient to provide predictions within 10% of the experimental results. Fig. 10a highlights the proximity between the ANN calculations and the experimental results, with most predictions having an error less than 10%. In fact, only 10.5% of the training data and 2.9% of the validation data had an absolute error larger than the 10% threshold. The results for the dimensionless PE4 charge impulse, $I_c/(m_c v_d)$, given by Fig. 10b further emphasise the ANN efficiency as it shows that the results of 97.14% of the validation dataset and the results of 85.96% of the training dataset lie within the $\pm\ 0.025 I_c/(m_c v_d)$ confidence interval. The complete ANN formulation, including the trained weights, is given in Appendix A.3.1.

Even though the validation dataset displayed a statistical distribution similar to the training population, as summarized by Table 5, the validation exercise provided superior results than the training exercise, a highly counterintuitive result. This behaviour was not expected from ANNs and can be explained by the existence of repeated experiments for certain charge sizes in the training population. About a third of the

Table 6
Limitations of the developed ANNs.

	Charge (PE4)		Plate (mild steel)			
	Height (mm)	**Diameter (mm)**	**Thickness (mm)**	**Breadth (mm)**	**Length (mm)**	**Static yield stress (MPa)**
Minimum	2.0	29.6	1.6	120.0	160.0	230.0
Maximum	8.6	64.0	3.0	190.6	294.4	288.0

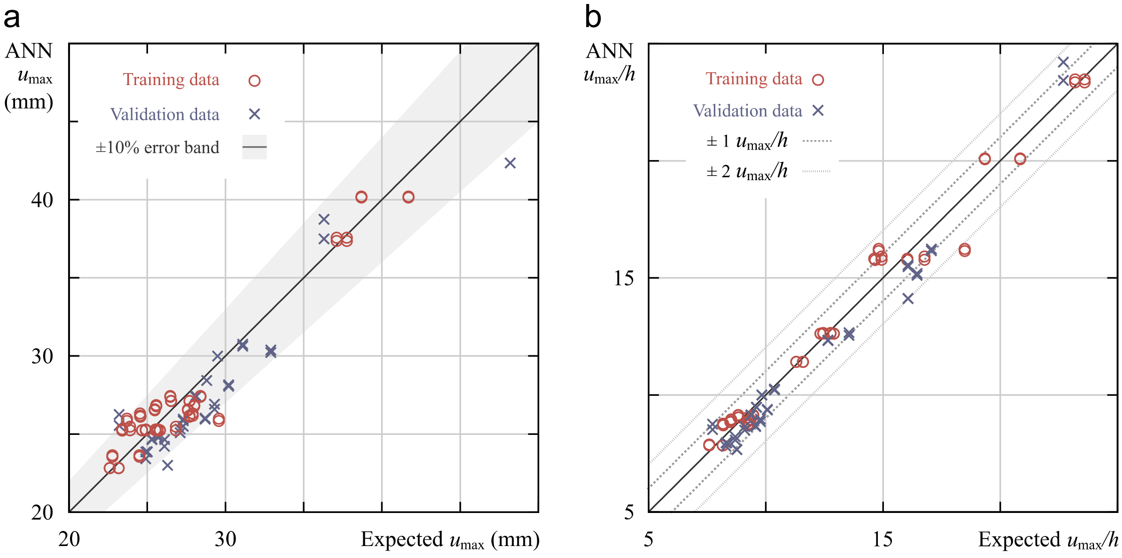

Fig. 14. Results from the ANN (ordinate) plotted against the expected values from the experiments (abscissa). The crosses indicate the data used for verifying the ANN whilst the circles represent the training samples. The effectiveness of the ANN is corroborated by the good agreement seen, with (a) many of the maximum mid-plate displacement $u_{\max}$ results falling within the ± 10% error band (shaded area) and (b) most of the plate mid-point deflection to thickness ratio $u_{\max}/h$ ANN results exhibit an absolute variation lower than $2u_{\max}/h$ when compared to the expected results.

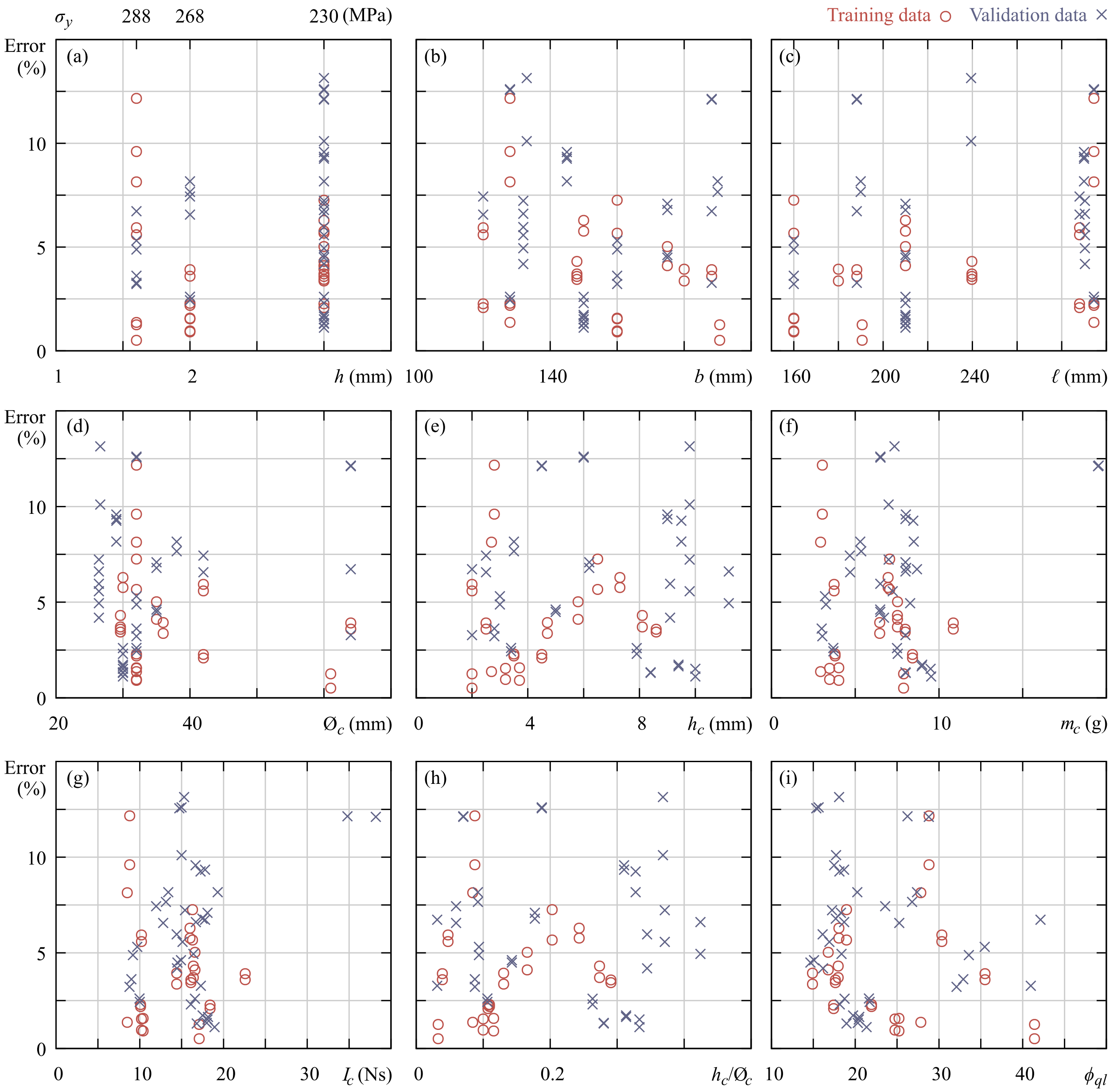

Fig. 15. Absolute ANN error to experiments distributed across the input domain for both training (circles) and validation data (crosses). Even though the (i) damage parameter ϕ_{ql} shows a well distributed training population at first, more training samples could lead to a more comprehensive ANN, especially for cases with: (a) plate thickness $h > 2$ mm, (b) plate breadth $b > 180$ mm, (c) plate length $\ell > 240$ mm, (d) charge diameter $\varnothing_c > 42$ mm, (e) charge height $h_c > 8$ mm, (f) charge mass $m_c > 11$ g, (g) charge impulse $I_c > 20$ Ns, or (h) charge aspect ratio $h_c/\varnothing_c > 0.3$.

training dataset are experimental repeats, which increased its statistical significance and provided for more accurate validation predictions albeit giving a poorer overall result. Fig. 11 illustrates the validation dataset distribution in comparison to the training population, as well as the ANN error observed.

The influence of the charge aspect ratio ($h_c/\varnothing_c$) on the impulse delivered is illustrated by Fig. 12. From this figure it can be observed that reducing $h_c/\varnothing_c$, i.e. giving the charge a flatter disc shape, will increase I_c. Most importantly, however, Fig. 12 demonstrates the ANN ability in finding reliable non-linear trends amongst the test data, which can be employed in predictive analyses, providing the limiting boundaries set by the training population are respected.

4.2. Maximum mid-plate displacement

A sensitivity study that varied the number of inputs and neurons in the hidden layer led to an ANN with eight inputs and eleven neurons (Fig. 13) to calculate the maximum mid-plate displacement ($u_{\max}$). Four of the inputs relate to the plate and the remaining four relate to the charge. The plate is represented by its dimensions (h, b, ℓ) and static yield stress (σ_y) whilst the charge is characterised by its mass (m_c), dimensions (h_c, $\varnothing_c$) and impulse (I_c). The empirical nature of the ANN (based on patterns found within the training data) means that the applicability is limited to the set of steel plates plastically deformed in “Mode Itc” as outlined by Jacob et al. [37]. All limiting parameters are listed in Table 6. Common elastic parameters such as the Young's modulus, Poisson's ratio or the shear modulus are not necessary in these models because they are constant for the entire database and would be disregarded by the training algorithm.

The data for training the model (Table 1) combined the experimental results and the FEA simulations in a so-called ‘replicative’ training. This approach doubled the training population to 30 samples,

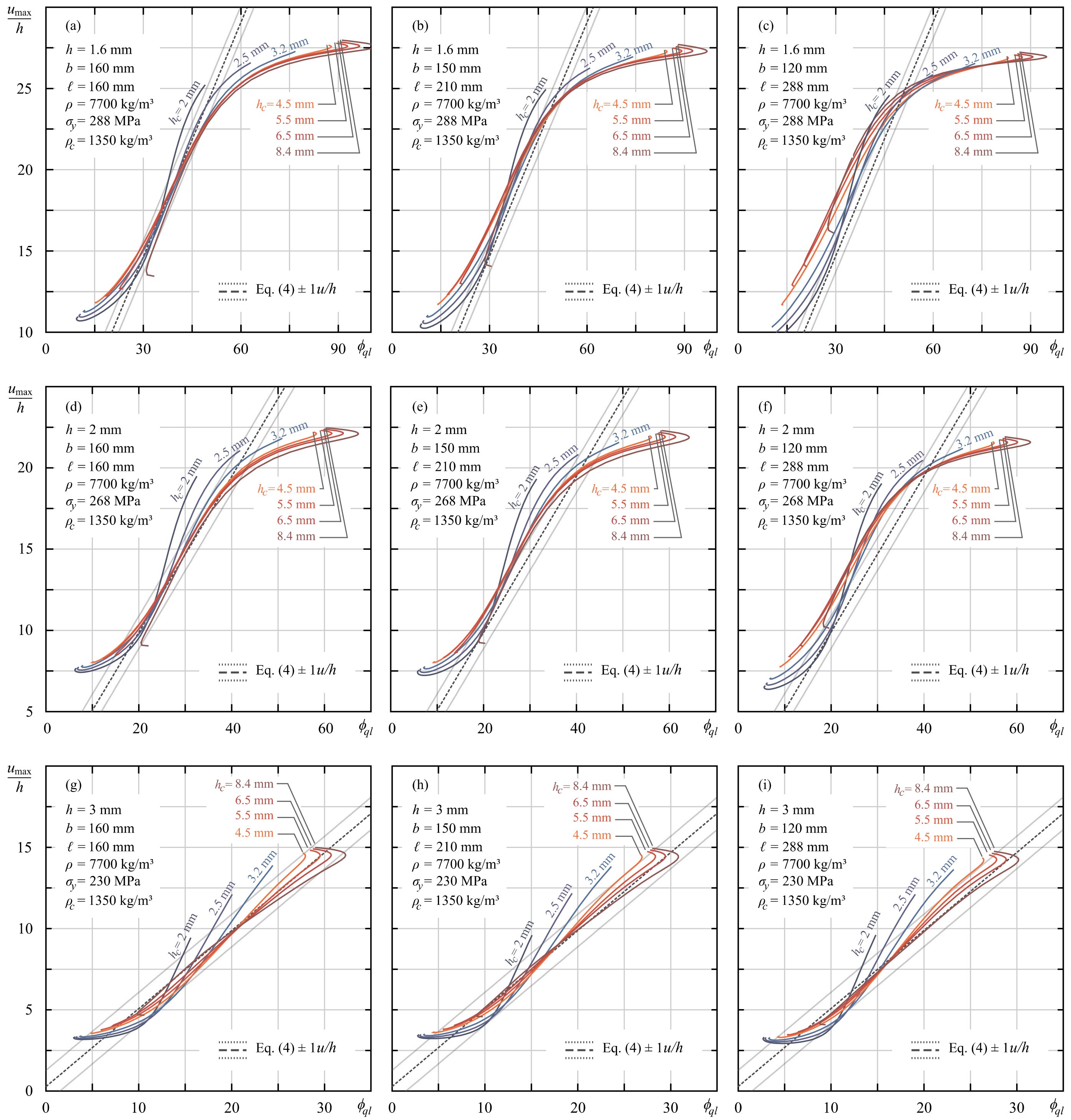

Fig. 16. Dimensionless damage parameter ϕ_{ql} versus the maximum mid-plate displacement–plate thickness ratio u_{max}/h for varying charge height h_c. Results for 1.6 mm (a–c), 2 mm (d–f) and 3 mm (g–i) thick plates of 160 × 160 mm (a,d,g), 150 × 210 mm (b,e,h) and 120 × 288 mm (c,f,i) are shown. The ANN (continuous lines) successfully captured the trends found on the experimental dataset, being consistent with the empirical relationship (5) (dashed line). However, care must be taken when employing this model to predictive analyses of situations not anticipated during the training stage as it starts to deviate from the expected behaviour.

adding noise to the u_{max} values owing to deviations between FEA and experimental results, as described in Section 3.2. This training method proved to be beneficial in increasing the ANN reliability. The remaining 20 specimens were set aside to validate the ANN. Appendix A.3.2 presents the scaling factors and trained weights. Fig. 14a shows that 10% of the validation data and 3.33% of the training data had an absolute error exceeding the 10% tolerance, highlighting the effectiveness of the model. The ANN results for the plate mid-point deflection to thickness ratio, u_{max}/h, are compared to the expected results in Fig. 14b, which shows that 77.5% of the validation data and 90% of the training data sit within the $\pm 1u_{max}/h$ confidence interval.

Fig. 15 illustrates the absolute ANN error to experimental results across the input domain, giving insights about gaps in the training data. It can be observed that an increased range of plate and charge dimensions in the training population is desirable as it would allow for a more comprehensive ANN. Furthermore, the inclusion of extra training

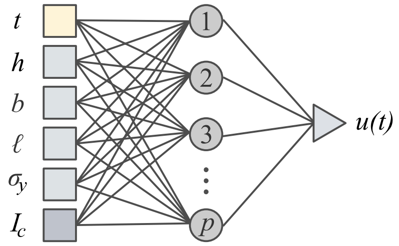

Fig. 17. ANN arrangement utilised for obtaining the transient mid-plate displacement $u(t)$. The plate dimensions (h, b, ℓ) and yield stress σ_y were combined to the charge impulse I_c to produce displacement estimates from time t= 0 to 300 µs. A varying number p of artificial neurons was used in the single hidden layer.

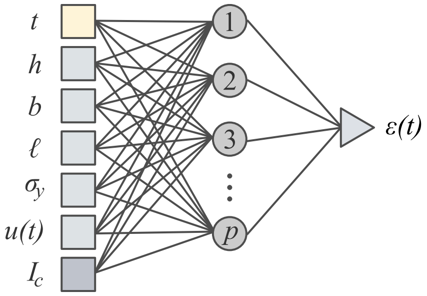

Fig. 18. ANN structure for obtaining the transient strain ε(t) at the centre of the plate. The plate dimensions (h, b, ℓ), mid displacement $u(t)$ and yield stress σ_y were combined to the charge impulse I_c to produce strain predictions from time t= 0 to 300 µs. A hidden layer with varying number p of artificial neurons was employed.

samples would potentially lead to more accurate predictions and expanded applicability.

Previous studies have demonstrated a linear correlation between the plate mid-point deflection to thickness ratio, i.e. $u_{\max}/h$, and the so-called damage parameter ϕ_{ql} [37,40]. An empirical relationship for predicting this ratio was presented by Nurick and Martin [40], which is expressed as:

$$\frac{u_{\max}}{h} = 0.48\phi_{ql} + 0.277. \tag{5}$$

This equation was originally developed for estimating the behaviour of quadrangular plates to uniform blast loads. It was later found that the equation above could also be employed to calculate $u_{\max}/h$ of plates subjected to localised blast loadings [37]. In this case the dimensionless damage parameter ϕ_{ql} takes the form:

$$\phi_{ql} = \frac{I_c}{2h^2}\left(1 + \ln\left(\frac{4}{\pi}\frac{\ell b}{\varnothing_c^2}\right)\right)\frac{1}{\sqrt{\ell b \rho \sigma_y}}. \tag{6}$$

A comparison between Eq. (5) and the ANN is given in Fig. 16 for varying charge height (h_c). This figure shows a tendency of the ANN to match the linear path of Eq. (5), demonstrating efficiency in learning the data pattern even with the small amount of training data available within the specified bounds. Conversely, as it is the case with most models, the ANN cannot operate beyond its limits as it may diverge from the expected trend. This is illustrated by the hairpin turns observed at the extremities of the ANN curves, Fig. 16, which are indicative of the unpredictable behaviour ANNs beyond the bounds of the training dataset. Designers and engineers must be mindful of this issue when employing models based on ANNs but this visual cue is highly useful is interrogating the ANN's results.

The strong deviation shown in Fig. 16 may allude to a strong material strength dependence whereby the ANN shows greater deviation for the 1.6 mm and 2 mm thick plates in comparison to the 3 mm thick plate. Not only has the ANN provided a good correlation to the empirical damage design space but the negative results at the outer damage limits highlights the errors associated with the simplified input of yield strength in its training as the scaled experiments exhibit a size effect associated with the thickness of the tested plates. The ANN may require greater refinement to account not only for the yield point but the post yield behaviour and flow stress. Future work will look to vary the JC parameters to better match the observed experimental displacements through an optimisation technique.

4.3. Transient mid-plate displacement and plastic strain

Following the development of ANNs for predicting the impulse generated by cylindrical PE4 charges and the maximum mid-plate displacement, the capacity of this technique in capturing temporal aspects of high strain-rate loadings was investigated. A dataset composed of 15 of the FEA simulations was utilised for training two multilayer perceptrons: one to obtain the transient mid-plate displacement ($u(t)$) and another to calculate the transient plastic strain (ε(t)) at the centre of the plate. The 5 remaining samples were saved to validate the model. Ideally, both training and validation datasets would be larger than this, but these serve as a proof of concept.

The ANN to compute the transient mid-plate displacement was structured as shown by Fig. 17. The input parameters focus on the plate dimensions (h, ℓ, b) and static yield stress (σ_y), the impulse (I_c) delivered by the cylindrical charge, and the time of interest (t). In addition to these parameters, the transient plastic strain ANN also requires the transient mid-plate displacement ($u(t)$), as illustrated by Fig. 18. To evaluate the influence of the artificial neurons on the performance of the ANNs, the number p of neurons in the hidden layer was varied from three up to fifteen ($3 \le p \le 15$). Similarly to the maximum mid-plate displacement ANN, the ANNs presented in this section are also limited by the training population, with most accurate predictions being within the data range displayed in Table 6 and $t \le$ 300 µs.

Figs. 19 and 21 compare the FEA results with the ANN outputs for the transient mid-plate displacement ($u(t)$) and the transient plastic strain (ε(t)) at the centre of the plate, respectively. Only the validation results are shown as it would be difficult to include the results for the complete training population. From these figures it can be observed that overall the ANNs produced reasonable predictions, with most curves falling within the ± 10% error band. From Figs. 20 and 22 it can be observed that high errors at small times, i.e. $t <$ 50 µs, as the ANN bias shifts the solution to satisfy other requirements of the training population. Inclusion of time dependent parameters, such as transient impulse and pressure, is likely to improve the overall ANN response. The models with $p = 12$ and $p = 15$ worked best for predicting the mid-plate displacement ($u(t)$) whereas the models with $p = 7$ and $p = 10$ yielded better curves for the transient plastic strain (ε(t)), as most of their predictions have revealed an absolute error lower than the absolute 10% tolerance highlighted in the graphs. Appendices A.3.3 and A.3.4 provide the reader with the scaling factors and trained weights respectively for the mid-plate displacement ANN with $p = 12$ and the mid-plate plastic strain ANN with $p = 7$.

This sensitivity study also demonstrates that increasing the number of artificial neurons does not directly translate into more accurate predictions and engineers must be careful to not generate over-trained models that might have poor generalisation capabilities [65]. It is worth noting that the ratio of hidden nodes to input required to achieving good correlation varies between ANNs. For time dependent variables, u

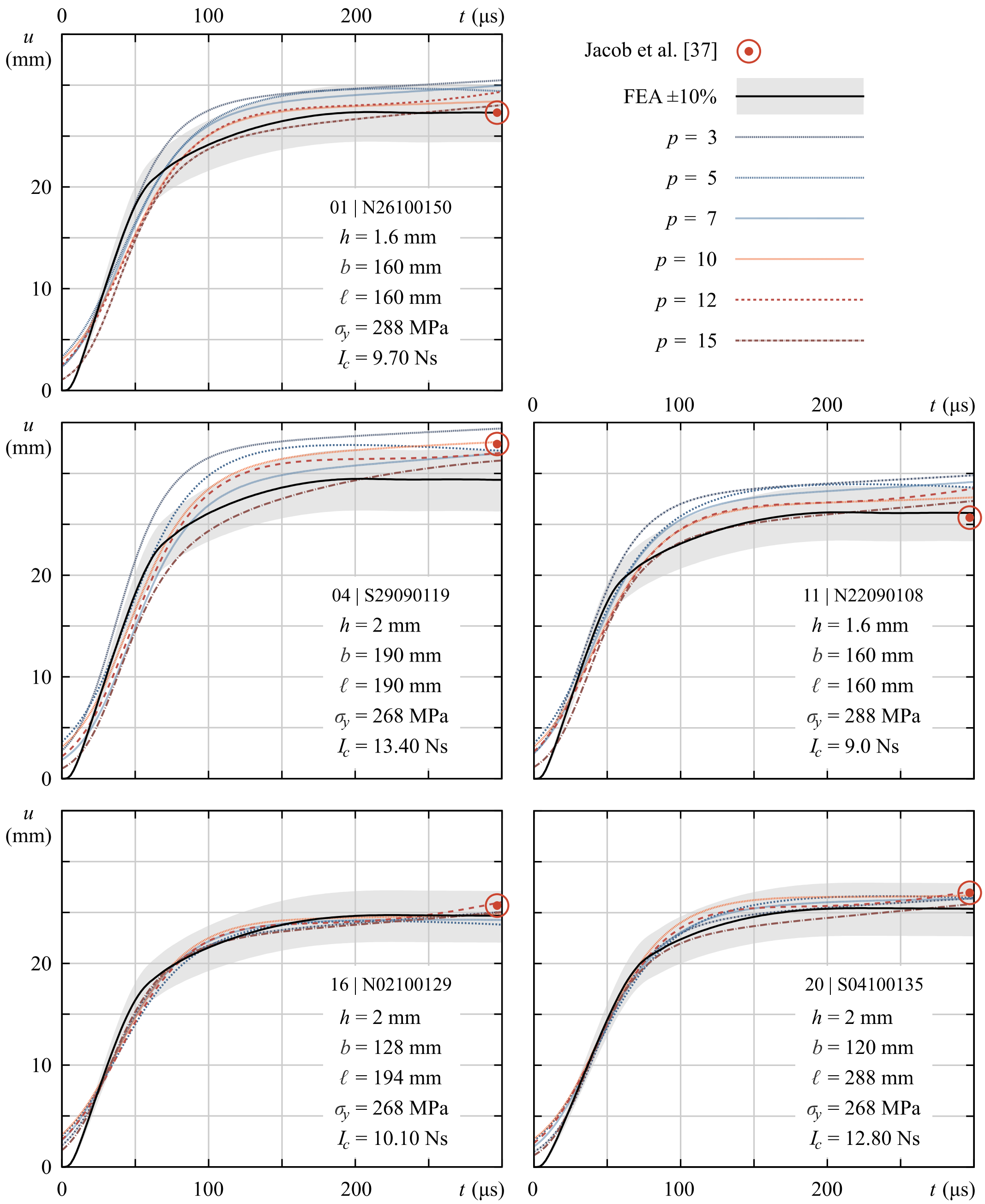

Fig. 19. Mid-plate displacement u over time t for five selected cases not used in the training of the ANNs. Outputs from ANNs with one hidden layer and varying number p of neurons are compared to FEA results. The maximum mid-plate displacement observed by Jacob et al. [37] is also included for comparison.

(t)) and ε(t), the ratio was 2:1, while for the Impulse and maximum displacement the ratio was closer to 4:3.

4.4. Limitations of the ANN models

The ANNs used herein incorporates limited physics in its foundation, as such it is not a first principles approach to the evaluation of blast interaction. The ANNs can be characterised as an empirical models or phenomenological models with the pattern recognition occurring by way of intrinsic weight functions. Some authors see these as a particular type of non-linear regression or classification model [66]. While this characteristic allows for swift developments of appropriate models it usually cannot be generalised and is constrained by the training population.

The sparseness of details in the experimental dataset utilised in this study thwarted the production of a ‘statistically representative subset’ that can be deduced from the broader 148 experiments of Jacobs et al. [37], Fig. 23. Such subsets, which are not used for training, validation or modelled using FEA, can be used to gauge response of the ANN to unknown conditions. To bypass this shortcoming, the study sought to compare the generated results of the ANNs against experimental points (charge impulse), empirical relationships (maximum mid-plate

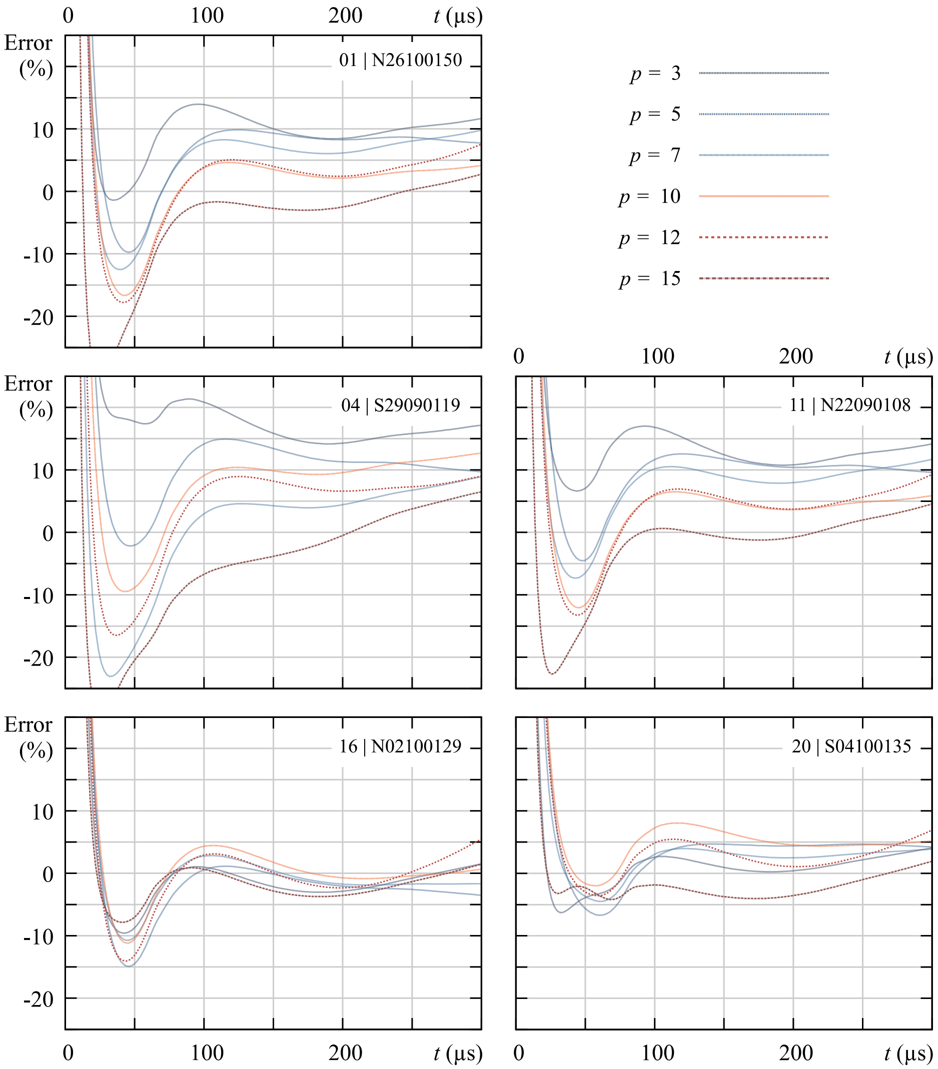

Fig. 20. ANN error to FEA for the transient mid-plate displacement $u(t)$ results. Five selected cases used in the validation process are shown for varying number p of artificial neurons.

displacement), and FEA models (temporal mid-plate displacement and strain). Another limitation imposed by the scarcity of the training population relates to plate and charge materials, dimensions and boundary conditions, as these features act to restrain the generalisation of the ANN solutions.

The stand-off distance is restricted to 12 mm, PE4 is the only charge composition accepted and the plate must be clamped and made of mild steel as the ANNs in their current form do not incorporate other material parameters. Table 6 lists the remaining limitations of the models. Moreover, because of the limited physical reasoning in the ANN computations, common elastic parameters – such as the Young's modulus, Poisson's ratio or shear modulus – are not required as these parameters are constant amongst the training data. Future developments could expand the options of plate dimensions and materials, boundary conditions, and charge compositions accepted.

5. Conclusion

The effectiveness of Artificial Neural Networks (ANNs) in delivering rapid and accurate predictions of the mechanical response of structures subjected to high strain-rate events was investigated focusing on clamped mild steel plates subjected to localised blast. ANNs were formulated to calculate the impulse delivered by cylindrical charges, the maximum displacement, the transient mid-plate displacement and the transient plastic strain at the centre of the plate.

As it is well known, experimental blast testing is inherently a low data environment with many attributes ill quantified owing to resource restrictions and the complex and severe blast testing environment. Physics based numerical simulations were conducted to provide additional data to supplement the ANN training and improve the validity and confidence in the final models. A 'replicative' training process was utilised whereby FE modelling results were used to bolster the experimental dataset used for training. The deviations amongst their results: (a) introduced noise and scatter in the data (within ~10%), (b) implicitly excluded experimental variation due to the idealised simulation setup and (c) increased the absolute number of training data points.

The ANNs developed were able to give reasonable predictions of the impulse delivered by cylindrical charges, the transient mid-plate displacement and the transient plastic strain at the centre of the plate, with generally good agreements being observed between the ANNs outputs and the experimental and numerical results. For time dependent variables, $u(t)$) and $\varepsilon(t)$, the ratio of hidden layers to inputs was found to be

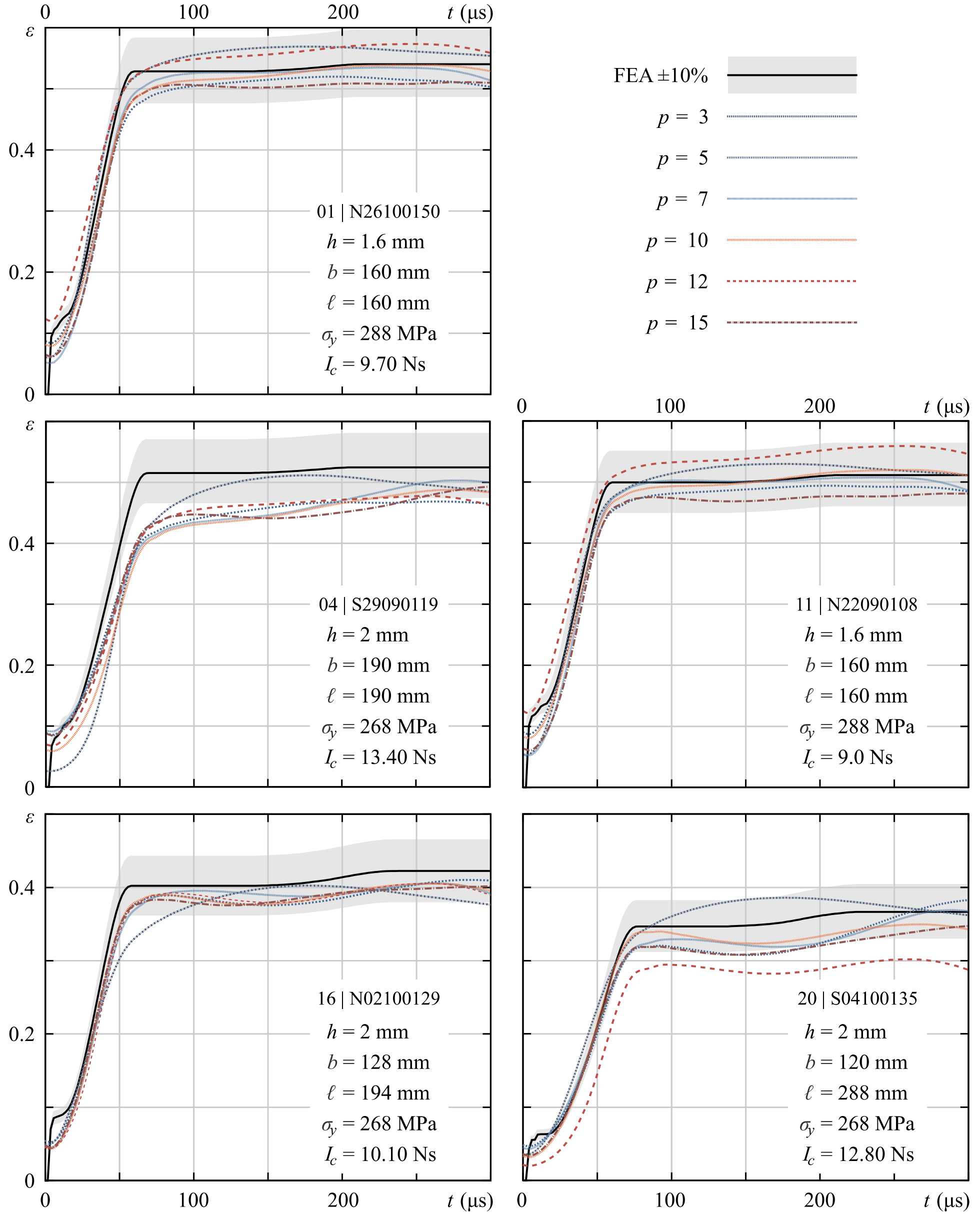

Fig. 21. Mid-plate plastic strain ε over time t for five selected cases not used in the training of the ANNs. FEA results are plotted against outputs from ANNs with a single hidden layer and varying number p of neurons.

approximately 2:1, while for the maximum Impulse and maximum displacement, time independent variables, the ratio was closer to 4:3.

The results also demonstrated the limitations of ANNs in predicting responses beyond the boundaries of the training dataset. This is an issue that engineers and designers must be conscious of when employing machine learning models in a predictive capacity. Also, supplementing experimental data with numerical modelling can improve the performance of ANNs, allowing for the inclusion of the material physical performance and the introduction of noise in the population dataset that aids the ANN in further recognising trends. Combining experiments, analytical tools, numerical models, and machine learning techniques can produce powerful frameworks for assessing the mechanical response of structures to blast events, allowing for the reduction of costs and resources associated to experimental setups and advanced numerical modelling.

As the ANNs developed here are applicable to mild steel plates and explosive charges of relatively small dimensions, the expansion of the current training population to include experimental data and/or FEA results of plates and charges of larger dimensions, varied boundary conditions and materials would allow for more comprehensive models. The methodology presented here could also be applied to more complex structures that might become subjected to high strain-rate deformation with appropriate boundary or simplification techniques. Future studies will look to investigate Support Vector Machines, Radial Basis Functions Networks or other machine learning techniques applied to simulate structural response to explosive threats, increasing the range of tools available to design engineers.

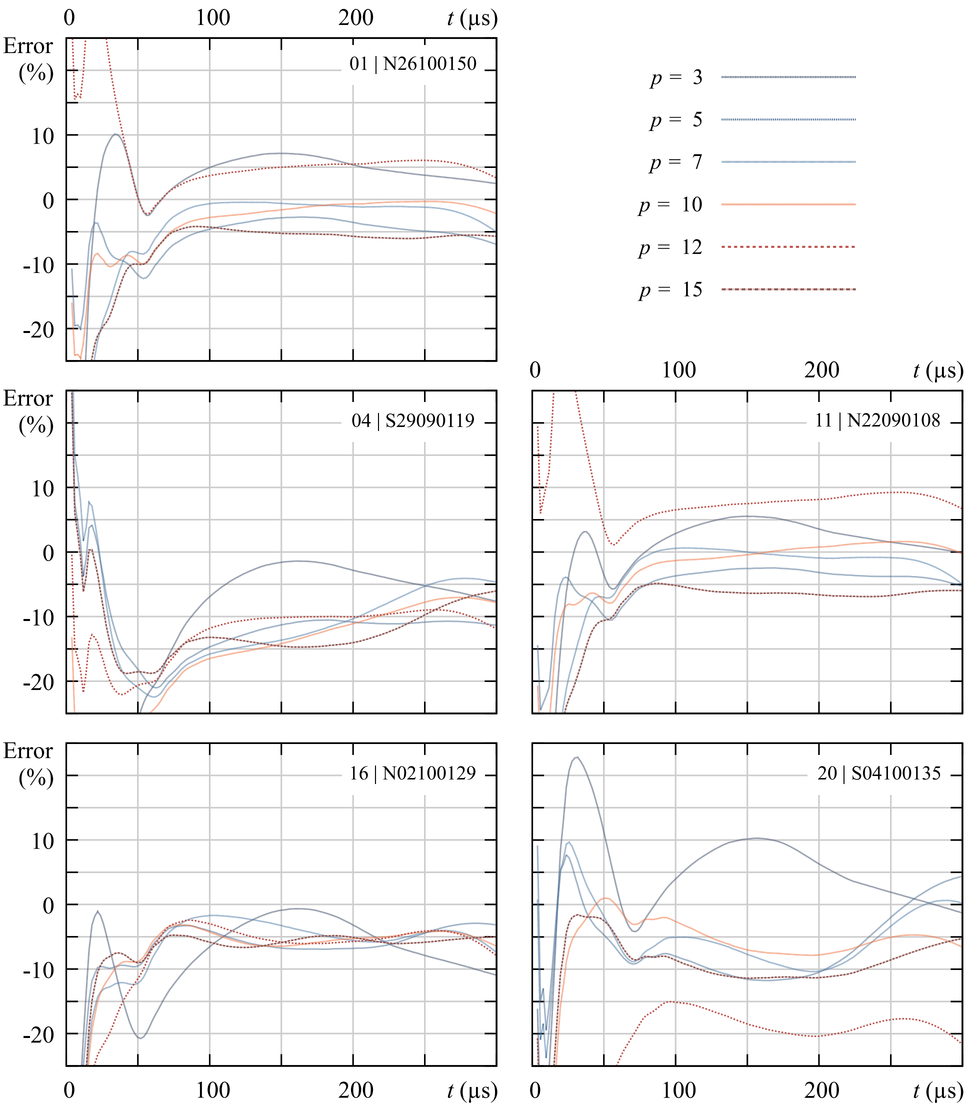

Fig. 22. ANN error to FEA transient mid-plate plastic strain ε(t) results. Five selected cases used in the validation process are shown for varying number p of artificial neurons.

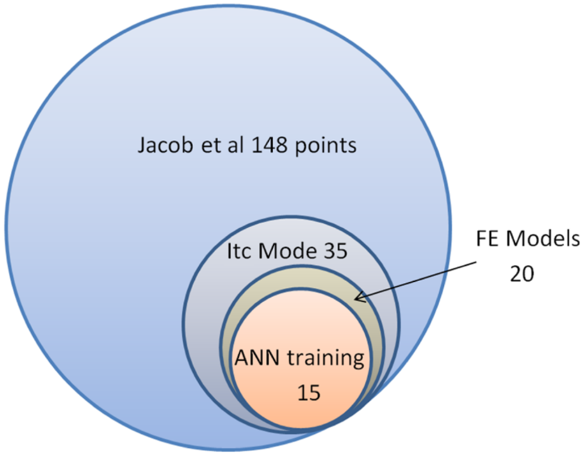

Fig. 23. Venn diagram of the ANN and FE cluster within the broader experimental set.

Declaration of Competing Interest

The authors declare that they have no known competing financial interests or personal relationships that could have appeared to influence the work reported in this paper.

Acknowledgments

This paper includes research that was supported by DMTC Limited (Australia). The authors have prepared this paper in accordance with the intellectual property rights granted to partners from the original DMTC project. The authors also wish to thank Dr Anthony Travers of DST group and the reviewers for their comments and helpful discussions and the IT department at ANSTO for the provision of high performance computing.

Supplementary materials

Supplementary material associated with this article can be found, in the online version, at doi:10.1016/j.ijimpeng.2019.103461.

Appendix A

A.1. The multilayer perceptron

In a classical work it was proposed that neurons could operate as switches which would be on or off depending on the input signals received [67]. From this concept a simple computational node capable of evaluating an input vector $\mathbf{x}$ against a thresholding function $f(\mathbf{x})$ and providing a single, binary output $\hat{y}$ was formulated and became known as the perceptron [68]. Further advances of perceptron introduced the so-called activation function $\alpha(\cdot)$ onto the product between the connecting weight vector $\mathbf{w}$ and the input vector giving rise to the artificial neuron, which is mathematically expressed as

$$f(\mathbf{x}) = \alpha(\mathbf{w}^T\mathbf{x} + w_0) = \alpha\left(\sum_{j=1}^{n} x_j w_j + w_0\right) = \hat{y} \tag{7}$$

where n is the number of inputs, $j = 1,\ 2 \ldots n$, and w_0 is a bias value that shifts the decision boundary away from the origin and is independent from the input vector. The connecting weight vector elements can be seen as expansion coefficients for a statistical curve fit, allowing for the system behaviour to be modelled through a linear combination of basic functions. The activation function $\alpha(\cdot)$ introduces nonlinearity in the models and usually has a sigmoid form, being commonly represented by the Heaviside step function, the logistic function or the hyperbolic tangent function [61].

The artificial neuron alone cannot handle non-linear (complex) classifications and operations, but it can be grouped with other neurons into a self-organising multilayered network arrangement to absorb memories and relationships implicit within a data environment. This arrangement is made of at least two sequentially nested functional layers with each consisting of one or more neurons. It has been very effective in recognising patterns amongst very high dimensional systems and has become known as the multilayer perceptron [69].

The representative multilayer perceptron architecture shown in Fig. A.1 illustrates the transformations being applied to the input signals passing through the hidden layers in a feed-forward manner. The output patterns from a given hidden layer becomes an intermediate pattern h_i, serving as an input pattern to the next layer where once again the net input and activation values are calculated to produce the output pattern h_{i+1}. The multilayer perceptron can also be described in matrix form. In this case, the n inputs of a problem can be grouped in a vector $\mathbf{x}$ defined as

$$\mathbf{x}^T = \{x_1\ x_2\ \ldots\ x_n\} \tag{8}$$

and the vector $\hat{\mathbf{y}}$ containing the m calculated outputs is given by

$$\hat{\mathbf{y}}^T = \{y_1\ y_2\ \ldots\ y_m\} \tag{9}$$

Setting up the ANN with a total of l hidden layers, each layer k ($k = 0, 1, 2, \ldots l$) will have a total number of p_k neurons. These indices define the architecture of the ANN and must be defined a priori. Each hidden layer k is defined by a vector $\mathbf{h}^{(k)}$, such that

$$\begin{aligned} \mathbf{h}^{(0)} &= \alpha_0\left(\begin{Bmatrix} 1 \\ \mathbf{x} \end{Bmatrix}\right) \quad k = 0,\ p_0 = n \\ \mathbf{h}^{(k)} &= \left\{h_0^{(k)}\ \ h_1^{(k)}\ \ h_2^{(k)}\ \ \cdots\ \ h_{p_k}^{(k)}\right\}^T \quad \text{for } k = 1,\ 2 \ldots l \end{aligned} \tag{10}$$

Note that each element $h_i^{(k)}$ ($i = 0, 1, 2\ldots\ p_k$) represents an artificial neuron and is calculated from Eq. (7). Hence, for a given layer k

$$\begin{aligned} h_0^{(k)} &= 1 \\ h_i^{(k)} &= \alpha_k(\mathbf{w}_i^{(k-1)T}\mathbf{h}^{(k-1)}) = \alpha_k\left(\textstyle\sum_{j=0}^{p_{k-1}} h_j^{(k-1)} w_{i,j}^{(k-1)}\right) \quad \text{for } i = 1,\ 2 \ldots p_k \end{aligned} \tag{11}$$

with $\alpha_k(\cdot)$ being the activation function at the hidden nodes of the layer k. The reason for $h_0^{(k)} = 1$ for each and every layer is to ensure the independence of the biases $w_{i,0}^{(k)}$ for every neuron i.

The linear transformation $\alpha_0(\cdot)$ applied to the augmented input vector $\{1\ \ \mathbf{x}\}^T$ in Eq. (10) is often utilised to scale the input data to a finite range – usually $h_i^{(0)} \in [-1, +1]$ – which turns the training process less difficult as it avoids negligible differences in the function output resulting from differences between very high or low values [70].

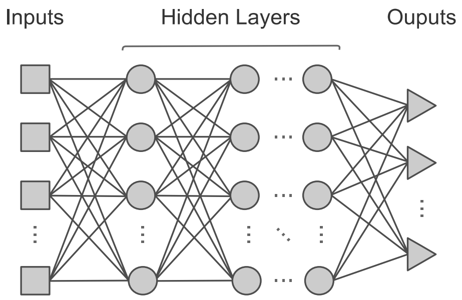

Fig. A.1. Schematic of the multilayer perceptron. In each layer the artificial neurons are arranged in parallel. Layers are processed in series and can have different numbers of neurons.

Combining the weight vectors $\mathbf{w}_i^{(k)}$ into a single weight matrix $\mathbf{W}_k$ of size $p_{k+1} \times (1 + p_k)$, Expression (11) can be rewritten as

$$\mathbf{h}^{(k)} = \alpha_k(\mathbf{W}_{k-1}\mathbf{h}^{(k-1)})\text{for } k = 1, 2...l \tag{12}$$

with

$$\mathbf{W}_k = \begin{bmatrix} \mathbf{w}_1^{(k)T} \\ \mathbf{w}_2^{(k)T} \\ \vdots \\ \mathbf{w}_i^{(k)T} \\ \vdots \\ \mathbf{w}_{p_{k+1}}^{(k)\ \ T} \end{bmatrix} = \begin{bmatrix} w_{1,0}^{(k)} & w_{1,1}^{(k)} & w_{1,2}^{(k)} & \dots & w_{1,j}^{(k)} & \dots & w_{1,p_k}^{(k)} \\ w_{2,0}^{(k)} & w_{2,1}^{(k)} & w_{2,2}^{(k)} & \dots & w_{2,j}^{(k)} & \dots & w_{2,p_k}^{(k)} \\ \vdots & \vdots & \vdots & \ddots & \vdots & \ddots & \vdots \\ w_{i,0}^{(k)} & w_{i,1}^{(k)} & w_{i,2}^{(k)} & \dots & w_{i,j}^{(k)} & \dots & w_{i,p_k}^{(k)} \\ \vdots & \vdots & \vdots & \ddots & \vdots & \ddots & \vdots \\ w_{p_{k+1},0}^{(k)} & w_{p_{k+1},1}^{(k)} & w_{p_{k+1},2}^{(k)} & \dots & w_{p_{k+1},j}^{(k)} & \dots & w_{p_{k+1},p_k}^{(k)} \end{bmatrix} \tag{13}$$

Note that the weight matrices $\mathbf{W}_0$, $\mathbf{W}_1$, ...$\mathbf{W}_l$ are basically linear maps of the activated outputs of the previous layer. The matrix form of the calculated output vector $\hat{\mathbf{y}}$ of the ANN is given by Eq. (14). In this equation, $g(\cdot)$ is the activation function at the output node.

$$\hat{\mathbf{y}} = g\left(\prod_{k=1}^{l} \mathbf{W}_k\mathbf{h}^{(k)}\right) = g\left(\mathbf{W}_l\alpha_l(\mathbf{W}_{l-1}\alpha_{l-1}(...\mathbf{W}_1\alpha_1(\mathbf{W}_0\mathbf{h}^{(0)})...))\right) \tag{14}$$

The error vector $\mathbf{e}$ is defined as the difference between the expected output $\mathbf{y}$ and the calculated output $\hat{\mathbf{y}}$, that is

$$\mathbf{e} = \mathbf{y} - \hat{\mathbf{y}}. \tag{15}$$

A.2. Training ANNs

Eq. (14) can be summarised as a weight function designed to give reliable approximations of the expected outputs. The problem now lies in determining the most suitable weights that will minimise the error between the expected results and the calculated ones. To address this issue, algorithms have been developed to automatically compute appropriate weights. This computation is commonly designated ANN training and can be classified as: supervised, unsupervised or reinforcement learning [71]. Supervised learning calls for a finite number of input samples with the respective outputs already known. Unsupervised learning consists of automatically finding equivalences within the dataset to cluster similar samples together. Reinforcement learning entails the testing of inputs and discovering which ones can produce the most rewarding outcomes. Most training algorithms work by iteratively adjusting initially random weights until either an error tolerance or another given constraint is met.

Predictive analyses of structural damage and vulnerability require reliable, pre-tested models capable of giving estimates with high levels of confidence. Supervised training algorithms are better suited for this task. Since the introduction of the backpropagation algorithm several methods of supervised training have been developed [72,73]. Examples of training schemes commonly employed include: quickprop [74], resilient propagation [75], Levenberg–Marquardt [58,59], and neuron-by-neuron [76,77] methods. The Levenberg–Marquardt algorithm is utilised in the current study due to its robustness and reliability. The origin of this algorithm dates back to the mid-twentieth century when Levenberg [78] and Marquardt [79] independently developed a curve-fitting method to solve non-linear least squares problems. This method was only applied to train neural networks in the mid-1990s [59], giving rise to the algorithm described in Fig. A.2. An in-depth description of the mathematical formulation behind this algorithm can be found in Yu and Wilamowski [80].

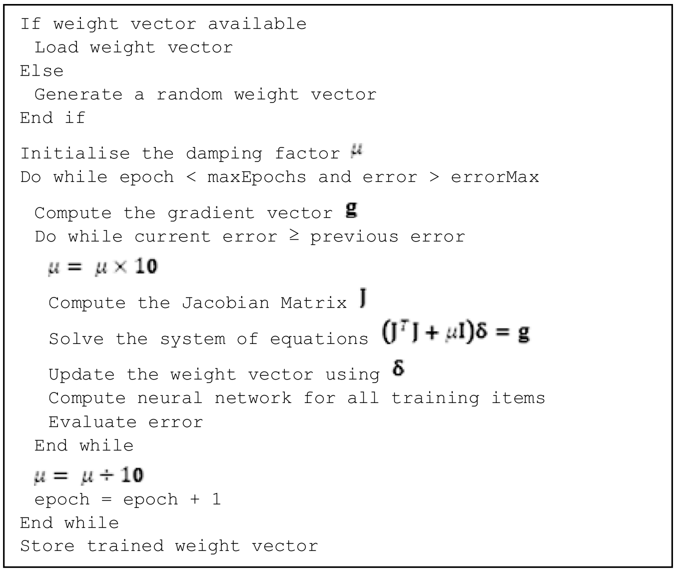

```
If weight vector available
  Load weight vector
Else
  Generate a random weight vector
End if

Initialise the damping factor $\mu$
Do while epoch < maxEpochs and error > errorMax

  Compute the gradient vector $\mathbf{g}$
  Do while current error ≥ previous error
    $\mu = \mu \times 10$
    Compute the Jacobian Matrix $\mathbf{J}$
    Solve the system of equations $(\mathbf{J}^T\mathbf{J} + \mu\mathbf{I})\boldsymbol{\delta} = \mathbf{g}$
    Update the weight vector using $\boldsymbol{\delta}$
    Compute neural network for all training items
    Evaluate error
  End while
  $\mu = \mu \div 10$
  epoch = epoch + 1
End while
Store trained weight vector
```

Fig. A.2. The Levenberg–Marquardt algorithm for training artificial neural networks.

A.3. ANNs with a single hidden layer and output

The general matrix form of an ANN for calculating the output vector $\hat{\mathbf{y}}$ was presented above in Eq. (14). For the particular case of ANNs with single hidden layer and one output the parameters l and m reduce to the unity, i.e. $l = m = 1$, and Eq. (14) can be rewritten as:

$$\hat{\mathbf{y}} = g(\mathbf{W}_1 \alpha_1 (\mathbf{W}_0 \mathbf{h}^{(0)})) \tag{16}$$

Normalisation of the input vector $\mathbf{x}$ and of the desired output $\mathbf{y}$ is usually performed to improve the training of ANNs. The desired outputs used for training the ANNs were normalised to [0, 1]. The required activation functions $\alpha_1(\cdot)$ and $g(\cdot)$ have a sigmoid form and were taken as:

$$\alpha_1(\cdot) = \begin{Bmatrix} 1 \\ \tanh(\cdot) \end{Bmatrix} \tag{17}$$

$$g(\cdot) = S\left(\frac{\exp(\cdot)}{\exp(\cdot) + 1}\right) \tag{18}$$

being S a factor for rescaling the calculated output from [0, 1] to the relevant magnitude.

The function $\alpha_0(\cdot)$ is a linear transformation applied to the augmented input vector $\{1 \;\; \mathbf{x}\}^T$ such that the elements of the transformed (scaled) input vector $\mathbf{h}^{(0)}$ range between [–1, +1]. The vector $\mathbf{h}^{(0)}$ can thus be calculated as

$$\mathbf{h}^{(0)} = \alpha_0\left(\begin{Bmatrix} 1 \\ \mathbf{x} \end{Bmatrix}\right) = \Lambda \begin{Bmatrix} 1 \\ \mathbf{x} \end{Bmatrix} \tag{19}$$

where $\mathbf{\Lambda}$ is a transformation matrix dependent from the input dataset. The elements of the weight matrices $\mathbf{W}_0$ and $\mathbf{W}_1$ are computed via a training scheme as detailed in Section A.2. The values taken by $\mathbf{h}^{(0)}$, $\mathbf{W}_0$, $\mathbf{W}_1$ and S for the ANNs described in Section 4 are given next.

A.3.1. Scaling factors and weights for the charge impulse ANN

The charge impulse ANN structure and performance were described in detail in Section 4.1. The transformed input vector $\mathbf{h}^{(0)}$ and the trained weight matrices $\mathbf{W}_0$ and $\mathbf{W}_1$ for the charge impulse ANN are given by Eqs. (20) to (22). The weight matrices $\mathbf{W}_0$ and $\mathbf{W}_1$ were calculated using the Levenberg–Marquardt algorithm, as described in Section A.2, with the training data being supplied by a normalised subset of the complete experimental dataset from Jacob et al. [37], as detailed in Section 4.1. The normalising factors in Table 7 are the overall maximum values of the training data increased by 10% which kept the training inputs within [–1, +1] and outputs within [0, 1]. This 10% difference was utilised in all ANN trainings to account for potential non-conforming data and experimental deviation as it provides a good engineering error margin. Substituting the values in Table 7 into Eq. (20) yields $\mathbf{h}^{(0)}$ for the charge impulse ANN. Eq. (16) can then be readily used for finding the charge impulse I_c when combined with Eqs. (17), (18), (20), (21), and (22) and $\hat{\mathbf{y}} = I_c$. The scaling factor S required for Eq. (18) is also listed in Table 7.

$$\mathbf{h}^{(0)} = \begin{Bmatrix} 1 \\ \dfrac{2\varnothing_c - \varnothing_{cmax}}{\varnothing_{cmax}} \\ \dfrac{2h_c - h_{cmax}}{h_{cmax}} \\ \dfrac{2m_c - m_{cmax}}{m_{cmax}} \end{Bmatrix} \tag{20}$$

$$\mathbf{W}_0 = \begin{bmatrix} -0.6510 & 1.2062 & 0.6824 & -0.8129 \\ 0.1735 & -0.0825 & 0.0755 & 0.8523 \\ -1.0155 & -0.0392 & -1.2167 & 0.8310 \\ -2.4121 & -1.2834 & -0.9647 & -0.9321 \end{bmatrix} \tag{21}$$

$$\mathbf{W}_1 = [-1.8089 \;\; -1.0100 \;\; 1.8066 \;\; 0.9910 \;\; -1.9672] \tag{22}$$

A.3.2. Scaling factors and weights for the maximum mid-plate displacement ANN

Section 4.2 introduced an ANN designed for calculating the maximum mid-plate displacement $u_{\max}$. Eqs. (23) to (25) give the transformed input vector $\mathbf{h}^{(0)}$ and the trained weight matrices $\mathbf{W}_0$ and $\mathbf{W}_1$, which can be readily utilised in Eq. (16) for calculating the approximate maximum mid-plate displacement by using $\hat{\mathbf{y}} = u_{\max}$. The computation of the weight matrices followed a ‘replicative’ training regime where a subset containing 15 experiments from Jacob et al. [37] (see Table 1) was complemented by corresponding FEA simulations. This increased dataset augmented the

Table 7
Scaling parameters for the charge impulse ANN.

Parameter	Symbol	Value	Unit
Maximum charge diameter	$\varnothing_{\text{cmax}}$	77.00	mm
Maximum charge height	h_{cmax}	13.86	mm
Maximum charge mass	m_{cmax}	21.494	g
Output scaling factor	S	39.27	–

Table 8
Scaling parameters for the maximum mid-plate displacement ANN.

Parameter	Symbol	Value	Unit	Parameter	Symbol	Value	Unit
Max. plate thickness	h_{max}	3.300	mm	Min. plate thickness	h_{min}	1.44	mm
Max. plate breadth	b_{max}	209.693	mm	Min. plate breadth	b_{min}	108.00	mm
Max. plate length	ℓ_{max}	323.840	mm	Min. plate length	ℓ_{min}	144.00	mm
Max. static yield stress	$\sigma_{y\text{max}}$	316.800	MPa	Min. static yield stress	$\sigma_{y\text{min}}$	207.00	MPa
Max. charge diameter	$\varnothing_{c\text{max}}$	70.400	mm	Max. charge mass	$m_{c\text{max}}$	11.946	g
Max. charge height	$h_{c\text{max}}$	9.460	mm	Max. charge impulse	$I_{c\text{max}}$	25.091	Ns
Output scaling factor	S	45.87	–				

training information available in Levenberg–Marquardt algorithm, resulting in the $\mathbf{W}_0$ and $\mathbf{W}_1$ values given by Eqs. (24) and (25). Once again the training inputs and outputs were respectively normalised to the ranges [–1, +1] and [0, 1]. The normalising parameters listed in Table 8 are the corresponding maximums/minimums of the training data increased/reduced by 10% (zero minimums were ignored). Substituting these parameters into Eq. (23) gives $\mathbf{h}^{(0)}$ necessary for the maximum mid-plate displacement ANN. The output scaling parameter S required for Eq. (18) is listed in Table 8. The maximum mid-plate displacement u_{max} is then computed by evaluating Eq. (16) using Eqs. (17), (18), (23), (24), and (25).

$$\mathbf{h}^{(0)} = \left\{\begin{matrix} 1 \\ \frac{2h - h_{max} - h_{min}}{h_{max} - h_{min}} \\ \frac{2b - b_{max} - b_{min}}{b_{max} - b_{min}} \\ \frac{2\ell - \ell_{max} - \ell_{min}}{\ell_{max} - \ell_{min}} \\ \frac{2\sigma_y - \sigma_{y_{max}} - \sigma_{y_{min}}}{\sigma_{y_{max}} - \sigma_{y_{min}}} \\ \frac{2\varnothing_c - \varnothing_{c_{max}}}{\varnothing_{c_{max}}} \\ \frac{2h_c - h_{c_{max}}}{h_{c_{max}}} \\ \frac{2m_c - m_{c_{max}}}{m_{c_{max}}} \\ \frac{2I_c - I_{c_{max}}}{I_{c_{max}}} \end{matrix}\right\} \tag{23}$$

$$\mathbf{W}_0 = \begin{bmatrix} -0.20982 & -0.57110 & 0.20511 & 0.29079 & 0.67115 & -0.19226 & -0.02314 & 0.75530 & 0.38843 \\ 0.24926 & 0.13909 & -0.16015 & 0.63091 & 0.83589 & 0.37392 & 0.36945 & -0.17702 & 0.12323 \\ 0.69944 & -0.08703 & 0.42451 & 0.13185 & -0.02504 & 0.05034 & 0.69567 & 0.40190 & -0.00536 \\ 0.34666 & -0.35396 & 0.39653 & 0.45777 & -0.36381 & 0.22754 & 0.80906 & 0.65260 & -0.05144 \\ -0.28962 & -0.30780 & 0.28373 & -0.32324 & -0.42078 & -0.31849 & 0.19812 & -0.23186 & -0.43581 \\ 0.04053 & -0.57375 & -0.61368 & 0.00275 & 0.30610 & -0.31210 & -0.63240 & 0.33577 & 0.02389 \\ 0.44410 & -0.15657 & 0.14306 & -0.40359 & 0.34801 & -0.38305 & 0.17530 & -0.39664 & -0.38619 \\ -0.69045 & 0.09094 & 0.08104 & -0.10411 & 0.49546 & 0.52878 & -0.36643 & -0.87778 & -0.17745 \\ 0.35603 & -0.31941 & -0.30402 & 0.15743 & -0.68316 & 0.00994 & -0.12579 & 0.46486 & 0.25302 \\ -0.39082 & 0.45832 & 0.25534 & -0.35958 & 0.39056 & -0.34224 & 0.20506 & -0.28748 & 0.13286 \\ -0.17800 & 0.29390 & -0.32806 & 0.06581 & 1.26816 & 0.17985 & 0.12680 & 0.43741 & 0.23849 \end{bmatrix} \tag{24}$$

$$\mathbf{W}_1^{\mathrm{T}} = \begin{bmatrix} -0.08070 \\ 0.56498 \\ -0.87025 \\ 0.55987 \\ 0.82217 \\ 0.17892 \\ 0.76026 \\ 0.17483 \\ -0.29625 \\ 0.29634 \\ -0.15033 \\ 0.53239 \end{bmatrix} \tag{25}$$

A.3.3. Scaling factors and weights for the transient mid-plate displacement ANN

Presented in Section 4.3, the transient mid-plate displacement ANN was exclusively trained using the results of 15 FEA simulations Section 3) that described the temporal displacement of the centre of the plate. Six ANN structures with varying number p of artificial neurons were compared. Eqs. (26) to ((28) show the transformed input vector $\mathbf{h}^{(0)}$ and the trained weight matrices $\mathbf{W}_0$ and $\mathbf{W}_1$ for the transient mid-plate displacement ANN with 12 artificial neurons in the hidden layer ($p = 12$). Training of $\mathbf{W}_0$ and $\mathbf{W}_1$ employed the Levenberg–Marquardt as described in Appendix A.2 with the training inputs being normalised to the interval [–1, +1] and the training outputs normalised to the range [0, 1]. Table 8 and Table 9

Table 9
Additional scaling parameters for the transient mid-plate displacement ANN.

Parameter	Symbol	Value	Unit
Maximum time	$t_{\max}$	0.3300231	ms
Max. charge impulse	$I_{c\max}$	24.86	Ns
Min. charge impulse	$I_{c\min}$	7.65	Ns
Output scaling factor	S	0.0426328	–

present the scaling parameters required for computing $\mathbf{h}^{(0)}$ using Eq. (26) and the output scaling parameter S necessary for Eq. (18). Note that parameters S and $I_{c\max}$ from Table 8 must be replaced by their counterparts listed in Table 9. The factors presented in Tables 8 and 9 are 10% larger/smaller than the maximum/minimum values observed in the training dataset (zero minimums were again ignored). The approximate transient mid-plate displacement $u(t)$ can then be calculated using $\hat{\mathbf{y}} = u(t)$ and solving Eq. (16) with Eqs. (17), (18), (26), (27) and (28).

$$\mathbf{h}^{(0)} = \left\{ \begin{matrix} 1 \\ \frac{2t - t_{max}}{t_{max}} \\ \frac{2h - h_{max} - h_{min}}{h_{max} - h_{min}} \\ \frac{2b - b_{max} - b_{min}}{b_{max} - b_{min}} \\ \frac{2\ell - \ell_{max} - \ell_{min}}{\ell_{max} - \ell_{min}} \\ \frac{2\sigma_y - \sigma_{y_{max}} - \sigma_{y_{min}}}{\sigma_{y_{max}} - \sigma_{y_{min}}} \\ \frac{2I_c - I_{c_{max}} - I_{c_{min}}}{I_{c_{max}} - I_{c_{min}}} \end{matrix} \right\} \tag{26}$$

$$\mathbf{W}_0 = \begin{bmatrix} -2.17692 & -2.30522 & 0.29114 & 0.14920 & -0.00586 & 0.68712 & 0.23737 \\ 0.78129 & -0.20046 & 0.90428 & -0.49223 & -0.22094 & 0.15149 & -0.14848 \\ 0.29209 & 0.72711 & 0.22377 & 0.43010 & -0.14693 & -0.66829 & 0.38706 \\ 0.26895 & 1.20766 & 0.00329 & -0.28988 & -0.19618 & -0.31487 & -0.11082 \\ -0.46526 & 0.41054 & 0.12559 & -0.47684 & 0.60525 & -0.27331 & -0.51970 \\ -0.59347 & -0.25533 & -0.35505 & 0.28025 & -0.26729 & 0.49774 & 0.71011 \\ 0.30508 & 0.27667 & 0.31368 & 0.39954 & -0.57513 & -0.34846 & 0.14707 \\ 0.21289 & 0.64098 & 0.27127 & -0.30257 & 0.14042 & 0.08143 & 0.21615 \\ 0.07769 & 1.16984 & 0.23941 & -0.37220 & 0.08786 & -0.52688 & -0.08357 \\ -0.35693 & -0.26539 & -0.18013 & 0.78770 & -0.02550 & -0.43476 & 0.25779 \\ -2.28304 & -2.49358 & -0.47304 & 0.07713 & 0.13235 & -0.10153 & 0.59633 \\ -0.32489 & -0.48974 & -0.28978 & 0.43421 & -0.32845 & -0.38673 & -0.52316 \end{bmatrix} \tag{27}$$

$$\mathbf{W}_1^T = \begin{bmatrix} -1.74351 \\ -1.16124 \\ 0.37119 \\ -0.44573 \\ -0.10831 \\ 0.55759 \\ 0.17387 \\ 0.15643 \\ -0.41238 \\ -0.22346 \\ -1.70198 \\ -0.78650 \\ -1.88471 \end{bmatrix} \tag{28}$$

A.3.4. Scaling factors and weights for the transient mid-plate plastic strain ANN

The transient mid-plate plastic strain ANN was exclusively trained using the results for the temporal plastic strain of the centre of the plate $\varepsilon(t)$ obtained from 15 FEA simulations Section 3). A comparison of six ANN structures with variable number p of artificial neurons was given in Section 4.3. Following the same procedure detailed in the sections above, these ANNs were trained with the Levenberg–Marquardt algorithm (Section A.2) and the training data was normalised to the [–1, +1] interval for the inputs and [0, 1] for the outputs. The normalising factors for the transformed input vector $\mathbf{h}^{(0)}$ are listed in Tables 8, 9 and 10 and were taken as each input maximum/minimum increased/decreased by 10%. Note that the parameters $I_{c\max}$ and S from Table 8 must be replaced by the corresponding values in Tables 9 and 10. The transformed input vector $\mathbf{h}^{(0)}$ and the trained weight matrices $\mathbf{W}_0$ and $\mathbf{W}_1$ for the ANN with seven artificial neurons in the hidden layer ($p = 7$) are given by Eqs. (29) to ((31). The output scaling parameter S listed in Table 10 is used in Eq. (18) to adjust the calculated output to the correct order of magnitude. With $\hat{\mathbf{y}} = \varepsilon(t)$ and combining Eq. (16) with Eqs. (17), (18), (29), (30), and (31) it is then possible to obtain the approximate temporal plastic strain of the centre of the plate.

Table 10
Additional scaling parameters for the transient mid-plate plastic strain ANN.

Parameter	Symbol	Value	Unit
Max. temporal displacement	$u(t)_{\max}$	43.112	mm
Output scaling factor	S	0.69076	–

$$\mathbf{h}^{(0)} = \left\{ \begin{array}{c} 1 \\ \frac{2t - t_{max}}{t_{max}} \\ \frac{2h - h_{max} - h_{min}}{h_{max} - h_{min}} \\ \frac{2b - b_{max} - b_{min}}{b_{max} - b_{min}} \\ \frac{2\ell - \ell_{max} - \ell_{min}}{\ell_{max} - \ell_{min}} \\ \frac{2\sigma_y - \sigma_{y_{max}} - \sigma_{y_{min}}}{\sigma_{y_{max}} - \sigma_{y_{min}}} \\ \frac{2I_c - I_{c_{max}} - I_{c_{min}}}{I_{c_{max}} - I_{c_{min}}} \\ \frac{2u(t) - u(t)_{max}}{u(t)_{max}} \end{array} \right\} \tag{29}$$

$$\mathbf{W}_0 = \begin{bmatrix} 0.04473 & -0.32599 & 0.56523 & -0.24042 & -0.59620 & -0.84992 & -0.26031 & 0.03886 \\ 0.12824 & -0.53719 & 0.49602 & -1.36136 & 0.20039 & 0.33070 & 0.02420 & 1.14094 \\ 1.02223 & -0.45390 & 0.40653 & 2.02439 & -0.68650 & -0.19208 & 0.08405 & 1.07149 \\ 0.90154 & -1.95455 & -0.29131 & -0.05239 & 0.06991 & -0.21028 & 0.25418 & -0.66007 \\ -0.69989 & 0.31243 & 0.16831 & -0.72145 & -0.14712 & -0.04005 & -0.15276 & -0.64323 \\ -0.48054 & -0.68739 & 0.10396 & 0.08600 & 0.18933 & -0.09679 & -0.44874 & 0.88262 \\ 0.19137 & -0.50630 & -0.27824 & -0.27485 & 0.42346 & 0.11125 & -0.25900 & -0.26540 \end{bmatrix} \tag{30}$$

$$\mathbf{W}_1 = [0.10031 \quad -0.70847 \quad 1.92626 \quad 1.83217 \quad -1.31620 \quad -0.68329 \quad 1.94947 \quad 0.28862] \tag{31}$$

References

[1] Langdon GS, Rossiter IB, Balden VH, Nurick GN. Performance of mild steel perforated plates as a blast wave mitigation technique: experimental and numerical investigation. Int J Impact Eng 2010;37:1021–36. https://doi.org/10.1016/j.ijimpeng.2010.06.001.

[2] Longère P, Geffroy A-G, Leblé B. Experimental and numerical aspects of ship structure failure under airblast loading. Proceedings of the EDP sciences, Freiburg, Germany 2012. p. 04003. https://doi.org/10.1051/epjconf/20122604003.

[3] Longère P, Geffroy-Grèze A-G, Leblé B, Dragon A. Ship structure steel plate failure under near-field air-blast loading: numerical simulations vs experiment. Int J Impact Eng 2013;62:88–98. https://doi.org/10.1016/j.ijimpeng.2013.06.009.

[4] Saleh M, Edwards L, Crouch IG, 9 Chapter. Numerical modelling and computer simulations. In: Crouch IG, editor. The science of Armour materials Cambridge, England: Woodhead Publishing; 2017. p. 483–579. https://doi.org/10.1016/B978-0-08-100704-4.00009-8.

[5] Saleh M, Luzin V, Toppler K, Kabir K. Response of thin-skinned sandwich panels to contact loading with flat-ended cylindrical punches: experiments, numerical simulations and neutron diffraction measurements. Compos Part B Eng 2015;78:415–30. https://doi.org/10.1016/j.compositesb.2015.04.001.

[6] Stewart LK. PhD Thesis, University of California. 2010.

[7] Avachat S, Zhou M. High-speed digital imaging and computational modeling of dynamic failure in composite structures subjected to underwater impulsive loads. Int J Impact Eng 2015;77:147–65. https://doi.org/10.1016/j.ijimpeng.2014.11.008.

[8] Langrand B, Leconte N, Menegazzi A, Millot T. Submarine hull integrity under blast loading. Int J Impact Eng 2009;36:1070–8. https://doi.org/10.1016/j.ijimpeng.2009.03.001.

[9] Micallef K, Fallah AS, Curtis PT, Louca LA. On the dynamic plastic response of steel membranes subjected to localised blast loading. Int J Impact Eng 2016;89:25–37. https://doi.org/10.1016/j.ijimpeng.2015.11.002.

[10] Yao S, Zhang D, Lu F, Chen X, Zhao P. A combined experimental and numerical investigation on the scaling laws for steel box structures subjected to internal blast loading. Int J Impact Eng 2017;102:36–46. https://doi.org/10.1016/j.ijimpeng.2016.12.003.

[11] Zheng C, Kong X, Wu W, Liu F. The elastic-plastic dynamic response of stiffened plates under confined blast load. Int J Impact Eng 2016;95:141–53. https://doi.org/10.1016/j.ijimpeng.2016.05.008.

[12] Ryan S, 8 Chapter. Analytical techniques and mathematical modelling. In: Crouch IG, editor. The science of Armour materials Cambridge, England: Woodhead Publishing; 2017. p. 395–481. https://doi.org/10.1016/B978-0-08-100704-4.00008-6.

[13] Feldgun VR, Yankelevsky DZ, Karinski YS. A nonlinear sdof model for blast response simulation of elastic thin rectangular plates. Int J Impact Eng 2016;88:172–88. https://doi.org/10.1016/j.ijimpeng.2015.09.001.

[14] Lee K, Shin J. Equivalent single-degree-of-freedom analysis for blast-resistant design. Int J Steel Struct. 2016;16:1263–71. https://doi.org/10.1007/s13296-016-0073-0.

[15] Rigby SE, Tyas A, Bennett T. Elastic–plastic response of plates subjected to cleared blast loads. Int J Impact Eng 2014;66:37–47. https://doi.org/10.1016/j.ijimpeng.2013.12.006.

[16] Bhadeshia HKDH. Neural networks in materials science. ISIJ Int 1999;39:966–79. https://doi.org/10.2355/isijinternational.39.966.

[17] Haque ME, Sudhakar KV. Prediction of corrosion–fatigue behavior of DP steel through artificial neural network. Int J Fatigue 2001;23:1–4. https://doi.org/10.1016/S0142-1123(00)00074-8.

[18] Iacoviello F, Iacoviello D, Cavallini M. Analysis of stress ratio effects on fatigue propagation in a sintered duplex steel by experimentation and artificial neural network approaches. Int J Fatigue 2004;26:819–28. https://doi.org/10.1016/j.ijfatigue.2004.01.004.

[19] Haque ME, Sudhakar KV. ANN back-propagation prediction model for fracture toughness in microalloy steel. Int J Fatigue 2002;24:1003–10. https://doi.org/10.1016/S0142-1123(01)00207-9.

[20] Dunne D, Tsuei H, Sterjovski Z. Artificial neural networks for modelling of the impact toughness of steel. ISIJ Int 2004;44:1599–607. https://doi.org/10.2355/isijinternational.44.1599.

[21] Liu J, Chang H, Hsu TY, Ruan X. Prediction of the flow stress of high-speed steel during hot deformation using a BP artificial neural network. J Mater Process Technol 2000;103:200–5. https://doi.org/10.1016/S0924-0136(99)00444-6.

[22] Phaniraj MP, Lahiri AK. The applicability of neural network model to predict flow stress for carbon steels. J Mater Process Technol 2003;141:219–27. https://doi.org/10.1016/S0924-0136(02)01123-8.

[23] Mandal S, Sivaprasad PV, Venugopal S, Murthy KPN. Artificial neural network modeling to evaluate and predict the deformation behavior of stainless steel type AISI 304L during hot torsion. Appl Soft Comput 2009;9:237–44. https://doi.org/10.1016/j.asoc.2008.03.016.

[24] Li H-Y, Wei D-D, Li Y-H, Wang X-F. Application of artificial neural network and constitutive equations to describe the hot compressive behavior of 28CrMnMoV steel. Mater Des 2012;35:557–62. https://doi.org/10.1016/j.matdes.2011.08.049.

[25] Haghdadi N, Zarei-Hanzaki A, Khalesian AR, Abedi HR. Artificial neural network modeling to predict the hot deformation behavior of an A356 aluminum alloy. Mater Des 2013;49:386–91. https://doi.org/10.1016/j.matdes.2012.12.082.

[26] Ryan S, Thaler S. Artificial neural networks for characterizing Whipple shield performance. Procedia Eng 2013;58:31–8. https://doi.org/10.1016/j.proeng.2013.05.006.

[27] Ryan S, Thaler S. Artificial neural networks for characterising Whipple shield performance. Int J Impact Eng 2013;56:61–70. https://doi.org/10.1016/j.ijimpeng.2012.10.011.

[28] Ryan S, Thaler S, Kandanaarachchi S. Machine learning methods for predicting the outcome of hypervelocity impact events. Expert Syst Appl 2016;45:23–39. https://doi.org/10.1016/j.eswa.2015.09.038.

[29] Remennikov AM, Mendis PA. Prediction of airblast loads in complex environments using artificial neural networks. WIT Press; 2006. p. 269–78. https://doi.org/10.2495/SU060271.

[30] Remennikov AM, Rose TA. Predicting the effectiveness of blast wall barriers using neural networks. Int J Impact Eng 2007;34:1907–23. https://doi.org/10.1016/j.ijimpeng.2006.11.003.

[31] Bewick B, Flood I, Chen Z. A neural-network model-based engineering tool for blast wall protection of structures. Int J Protect Struct 2011;2:159–76. https://doi.org/10.1260/2041-4196.2.2.159.

[32] Flood I, Bewick BT, Dinan RJ. A new method for very fast simulation of blast wave propagation in complex built environments. In: Tizani W, editor. Computing in civil and building engineering, proceedings of the international conference. Nottingham, England: Nottingham University Press; 2010. p. 53–62 Paper 27 http://www.engineering.nottingham.ac.uk/icccbe/proceedings/pdf/pf27.pdf accessed September 7, 2018.

[33] Flood I, Bewick BT, Dinan RJ, Salim HA. Modeling blast wave propagation using artificial neural network methods. Adv Eng Inf 2009;23:418–23. https://doi.org/10.1016/j.aei.2009.06.005.

[34] Flood I, Bewick BT, Rauch E. Rapid simulation of blast wave propagation in built environments using coarse-grain based intelligent modeling methods. Defense Technical Information Center, Fort Belvoir, VA; 2011. https://doi.org/10.21236/ADA543599.

[35] Ibrahim A, Salim H, Flood I. Damage prediction for rc slabs under near-field blasts using artificial neural network. Int J Protect Struct 2011;2:315–32. https://doi.org/10.1260/2041-4196.2.3.315.

[36] Stewart LK, Morrill KB. Residual capacity prediction of blast-loaded steel columns using physics-based fast running models. Int J Saf Secur Eng 2015;5:289–303. https://doi.org/10.2495/SAFE-V5-N4-289-303.

[37] Jacob N, Chung Kim Yuen S, Nurick GN, Bonorchis D, Desai SA, Tait D. Scaling aspects of quadrangular plates subjected to localised blast loads—experiments and predictions. Int J Impact Eng 2004;30:1179–208. https://doi.org/10.1016/j.ijimpeng.2004.03.012.

[38] Rajendran R, Lee JM. Blast loaded plates. Marine Struct 2009;22:99–127. https://doi.org/10.1016/j.marstruc.2008.04.001.

[39] Nurick GN, Martin JB. Deformation of thin plates subjected to impulsive loading - A review part I: theoretical considerations. Int J Impact Eng 1989;8:159–70. https://doi.org/10.1016/0734-743X(89)90014-6.

[40] Nurick GN, Martin JB. Deformation of thin plates subjected to impulsive loading - A review part II: experimental studies. Int J Impact Eng 1989;8:171–86. https://doi.org/10.1016/0734-743X(89)90015-8.

[41] Pickerd V, Bornstein H, McCarthy P, Buckland M. Analysis of the structural response and failure of containers subjected to internal blast loading. Int J Impact Eng 2016;95:40–53. https://doi.org/10.1016/j.ijimpeng.2016.04.010.

[42] Pickerd VL. Optimisation and validation of the ARAMIS digital image correlation system for use in large-scale high-strain-rate events. Defence Science and Technology Organisation, Melbourne, Australia; 2013.

[43] Pickerd VL, Buckland M, McCarthy P, Yiannakopoulos G. Use of 3D image correlation for assessment of damage to mild steel containers subjected to internal blast loading and fragmentation events. Proceedings of the MABS 22. Bourges, France: MABS Executive Committee; 2012. p. 14.

[44] Pickerd VL, McCarthy PW. Damage of welded structures from internal explosive loading. In: Stewart MG, Netherton MD, editors. Proceedings of the 3rd international conference on protective structures (ICPS3). Newcastle, Australia: International Association of Protective Structures; 2015. p. 419–26.

[45] Bortolan Neto L, Saleh M, Pickerd V, Yiannakopoulos G, Mathys Z, Reid W. Rapid vulnerability assessment of naval structures subjected to localised blast. Proceedings of Pacific IMC, The Royal Institution of Naval Architects, The Institute of Marine Engineering, Science and Technology and Engineers Australia, Sydney, Australia. 2017. p. 12.

[46] Johnson GR, Cook WH. A constitutive model and data for metals subjected to large strains, high strain rates and high temperatures. Proceedings of the seventh international symposium on ballistic. Netherlands: The Hague; 1983. p. 541–7.

[47] Vedantam K, Bajaj D, Brar NS, Hill S. Johnson - cook strength models for mild and DP 590 steels. Proceedings of the AIP conference 845. 2006. p. 775–8. https://doi.org/10.1063/1.2263437.

[48] Saleh M, Edwards L. Numerical fe modelling of occupant injury in soil-vehicle blast interaction. Proceeding of the 28th international symposium on ballistics. Atlanta, Georgia: International Ballistics Society; 2014.

[49] Saleh M, Edwards L. Evaluation of a hydrocode in modelling nato threats against steel armour. Proceeding of the 25th international symposium on ballistics. Beijing, China: International Ballistics Committee; 2010.

[50] Saleh M, Edwards L. Application of a soil model in the numerical analysis of landmine interaction with protective structures. Proceeding of the ballistics 2011: 26th international symposium. Miami, Florida: DEStech Publications; 2011. p. 265–76.

[51] Saleh M, Edwards L. Evaluation of soil and fluid structure interaction in blast modelling of the flying plate test. Comput Struct 2015;151:96–114. https://doi.org/10.1016/j.compstruc.2015.01.010.

[52] Explosive effects and applications. In: Zukas JA, Walters WP, editors. Explosive effects and applications New York: Springer; 1998. https://doi.org/10.1007/978-1-4612-0589-0.

[53] Rigby SE, Sielicki PW. An investigation of tnt equivalence of hemispherical PE4 charges. Eng Trans 2014;4:423–35.

[54] Saleh M, Kariem MM, Luzin V, Toppler K, Li H, Ruan D. High strain rate deformation of ARMOX 500T and effects on texture development using neutron diffraction techniques and SHPB testing. Mater Sci Eng A 2018;709:30–9. https://doi.org/10.1016/j.msea.2017.09.022.

[55] Knock C, Davies N. Blast waves from cylindrical charges. Shock Waves 2013;23:337–43. https://doi.org/10.1007/s00193-013-0438-7.

[56] Hammond L. Underwater shock wave characteristics of cylindrical charges. Melbourne, Australia: Defence Science and Technology Organisation; 1995.

[57] Bortolan Neto L, Saleh M, Pickerd V, Yiannakopoulos G, Mathys Z, Reid W. Rapid assessment of structures subjected to localised blast. Proceedings of the MABS 25. Netherlands: The Hague; 2018. 12.Paper P – 079.

[58] More JJ. The Levenberg–Marquardt algorithm: implementation and theory. In: Watson GA, editor. Proceedings of the biennial conference numerical analysis: Held at Dundee, Scotland. Berlin, Germany: Springer; 1978. p. 105–16. June 28-July 1, 1977.

[59] Hagan MT, Menhaj MB. Training feedforward networks with the Marquardt algorithm. IEEE Trans Neural Netw 1994;5:989–93. https://doi.org/10.1109/72.329697.

[60] Hastie T, Tibshirani R, Friedman J. The elements of statistical learning: data mining, inference, and prediction. 2nd New York: Springer; 2009http://www.springerlink.com/index/10.1007/b94608 accessed July 27, 2016.

[61] Bishop CM. Neural networks for pattern recognition. Oxford, England: Clarendon Press; 1995.

[62] Neural networks: methodology and applications. In: Dreyfus G, editor. Neural networks: methodology and applications Berlin, Germany: Springer; 2005. https://doi.org/10.1007/3-540-28847-3.

[63] Haykin S. Networks Networks: A comprehensive foundation. 2nd New York: Pearson Education; 1999.

[64] Müller B, Reinhardt J, Strickland MT. Networks Networks: An introduction. 2nd Berlin, Germany: Springer; 1995. https://doi.org/10.1007/978-3-642-57760-4.

[65] Tzafestas SG, Dalianis PJ, Anthopoulos G. On the overtraining phenomenon of backpropagation neural networks. Math Comput Simul 1996;40:507–21. https://doi.org/10.1016/0378-4754(95)00003-8.

[66] Titterington DM. Bayesian methods for neural networks and related models. Stat Sci 2004;19:128–39. https://doi.org/10.1214/088342304000000099.

[67] McCulloch WS, Pitts W. A logical calculus of the ideas immanent in nervous activity. Bull Math Biophys 1943;5:115–33. https://doi.org/10.1007/BF02478259.

[68] Rosenblatt F. The perceptron: a probabilistic model for information storage and organization in the brain. Psychol Rev 1958;65:386–408. https://doi.org/10.1037/h0042519.

[69] Krogh A. What are artificial neural networks? Nat Biotech 2008;26:195–7. https://doi.org/10.1038/nbt1386.

[70] Chojaczyk AA, Teixeira AP, Neves LC, Cardoso JB, Guedes Soares C. Review and application of Artificial Neural Networks models in reliability analysis of steel structures. Struct Saf 2015;52:78–89. https://doi.org/10.1016/j.strusafe.2014.09.002.

[71] Sutton RS, Barto AG. Reinforcement learning: an introduction. 2nd Cambridge, Massachusetts: MIT Press; 2017.

[72] Schmidhuber J. Deep learning in neural networks: an overview. Neural Networks 2015;61:85–117. https://doi.org/10.1016/j.neunet.2014.09.003.

[73] Yaghini M, Khoshraftar MM, Fallahi M. A hybrid algorithm for artificial neural network training. Eng Appl Artif Intell 2013;26:293–301. https://doi.org/10.1016/j.engappai.2012.01.023.

[74] S.E. Fahlman, An empirical study of learning speed in back-propagation networks, School of Computer Science, Carnegie Mellon University, Pittsburgh, Pennsylvania, 1988.

[75] Riedmiller M, Braun H. A direct adaptive method for faster backpropagation learning: the RPROP algorithm. Proceedings of the IEEE international conference on neural networks. 1993. p. 586–91.

[76] Wilamowski BM, Cotton NJ, Kaynak O, Dundar G. Computing gradient vector and Jacobian matrix in arbitrarily connected neural networks. IEEE Trans Ind Electron 2008;55:3784–90. https://doi.org/10.1109/TIE.2008.2003319.

[77] Wilamowski BM, Yu H, Cotton N. Chapter 13: NBN algorithm. In: Wilamowski BM, Irwin JD, editors. Intelligent systems. 2ndBoca Raton, Florida: CRC Press; 2011. p. 24.

[78] Levenberg K. A method for the solution of certain non-linear problems in least squares. Q Appl Math 1944;2:164–8.

[79] Marquardt DW. An algorithm for least-squares estimation of nonlinear parameters. J Soc Ind Appl Math 1963;11:431–41. https://doi.org/10.1137/0111030.

[80] Yu H, Wilamowski BM. Chapter 12: Levenberg–Marquardt training. In: Wilamowski BM, Irwin JD, editors. Intelligent systems. 2ndBoca Raton, Florida: CRC Press; 2011. p. 16.